



**Universitat Autònoma
de Barcelona**

Bachelor Thesis

Bachelor's Degree in Physics

**Neural network dynamics
underlying biased perception in
motion discrimination tasks**

Miguel Donderis de Vicente

Supervisors

Klaus Wimmer, Daniel Campos

Year

2021/2022

Call

September

Abstract	v
1 Introduction	1
1.1 Neural Field models	1
1.2 Linear stability analysis of the effective model	3
1.3 Spatially inhomogeneous bump state patterns	4
2 Stimulus estimation with attractor dynamics	7
2.1 Single population ring model	7
2.2 Derivation of the amplitude equation	8
2.2.1 Spatially homogeneous perturbation	9
2.2.2 Spatially inhomogeneous perturbation	14
3 Modeling the Jazayeri-Movshon experiment	23
4 Conclusions	27
A Mathematical appendix	29
A.1 Taylor series of the transfer function	29
A.1.1 Homogeneous input	29
A.1.2 First order Fourier spatially inhomogeneous perturbation	30
A.1.3 Second order Fourier spatially inhomogeneous perturbation	31
A.1.4 Third order Fourier spatially inhomogeneous perturbation	31
A.1.5 Fourth order Fourier spatially inhomogeneous perturbation	33
A.2 Amplitude equation for a Fourth order Fourier input	36
A.2.1 Derivation of the amplitude equation	36
A.2.2 Dynamics of the amplitude equation	38

B Jazayeri-Movshon experiment psychophysical results	39
C Additional simulation results	43
D Code	51

Perceptual decision tasks and the continuous estimation of different stimulus orientation involve making decisions that are based on previous sensory evidence that a subject has accumulated. Neural network models of evidence integration are often based on competition between neural populations, each encoding a discrete categorical choice but this models do not maintain information that is necessary for a continuous perceptual judgement. In [3], the authors showed that a continuous attractor network could integrate a circular stimulus feature and track the stimulus average in the phase of its activity bump. Throughout this thesis we will study this kind of attractor networks and more specifically how does it integrate different Fourier order spatially modulated inputs. With this purpose, we will perform a multiple scale analysis, followed by a perturbation method, so as to derive the amplitude equation of the bump, a complex-valued magnitude that can be splitted into a real amplitude and a phase, the latter being the one we want to analyse deeper.

On the other hand, in the year 2007 the neuroscientists Mehrdad Jazayeri and Anthony Movshon carried out an experiment and proposed an encoding-decoding model so as to explain the post decision bias that six different subjects showed in their estimation of the orientation of a stimulus after performing a fine discrimination task. However, it remains unknown what kind of neural mechanisms give rise to this bias, so our second goal will be to study how does this continuous attractor model integrate one particular case of the previous higher Fourier order modulated input, consisting on a second order input with stable fixed points $\frac{\pi}{2}$, that will help the network force a decision.

CHAPTER 1

Introduction

We live in a continuous world, where all our movements and gestures can be described by continuous variables such as position, head direction, gaze orientation... Necessarily, these continuous variables need to be somehow represented in the brain activity, where everything begins. In neuroscience, the type of models that are used to encode such continuous variables are called *Neural Field* models, which describe the activity of local groups of cortical neurons and which exploit the idea that neighbouring neurons have very similar properties so as to arrive at a continuum model of the cortical, from the visual cortex, neural activity. That is why neural continuum models are often called field models. The neurons in this type of models typically receive input on a forward path, from sensory modalities such as vision, audition, or touch, but they also interact with each other, what will be a critical fact in our study. Neural field models have been very successful in explaining aspects of cortical circuits and perception, such as in [1] among others. Following recent work [3], we study here how they can accumulate information over time in order to enable perceptual estimation and decision making. With the purpose of introducing the bump attractor model that we will study deeply in this thesis we will make a brief review of the traditional field models following [2] and also reviewing different concepts from [4], which can be followed for a much more detailed derivation of all concepts.

1.1 Neural Field models

Since the appearance of the first computational neuroscience models describing the dynamics of single neurons in the visual cortex, networks of large number of spiking neurons have been the natural framework for studying dynamics of these cortical neu-

rons. Although their derivation includes the most important physiological elements and are generally considered to be biologically realistic models, given the immense number of neurons found in any small region of the cortex, network models are generally unpractical and time consuming.

This paradigm motivated many researchers to develop continuum theories of brain organization in an attempt to reduce the enormous complexity of neuronal interactions to simpler, macroscopic models that could become analytically tractable. The resulting mathematical models of cortical tissue are often referred to as *Neural Field* models, and they are generally presented as simple, phenomenological models of neuronal activity in the form of continuous, first-order differential equations, such as in [10].

In order to better understand these concepts, we now present the Wilson and Cowan model presented in [10], very often considered as the canonical neural field model, to which we will refer as the WC model. The simplest form of the WC equations describes the activity of the interacting excitatory and inhibitory sub-populations of neurons in terms of their respective firing rates, r_α , $\alpha = e, i$, where the different subscript makes reference to the excitatory or inhibitory nature of the neuron. Hence,

$$\begin{aligned}\tau_e \frac{\partial r_e}{\partial t} &= -r_e + \Phi(\tau_e J_{ee} r_e - \tau_e J_{ie} r_i + \eta_e + P_e(t)) \\ \tau_i \frac{\partial r_i}{\partial t} &= -r_i + \Phi(\tau_i J_{ei} r_e - \tau_i J_{ii} r_i + \eta_i + P_i(t)),\end{aligned}\tag{1.1}$$

where τ is a time constant determining the temporal scale of the dynamics of each sub-population and $\Phi(I)$ is the steady-state current-to-rate transfer function, or also know as f-I function.

The above equations describe the dynamics of local populations of neurons, the purpose of which is to model neural ensembles containing similar type of neurons located at specific places of the brain, for instance at the different layers of the cortical columns. However, a great deal of electrophysiological and anatomical data indicates that the cerebral cortex is spatially and functionally organized. Therefore, *Neural Field* models represent the natural extension of the above equations, where neuronal interactions, and consequently the activity of the neurons, are spatially dependent. They typically consist on a couple of partial integrodifferential equations describing the temporal and spatially dependent activity of populations of excitatory and inhibitory neurons. However, analytically dealing with partial differential equations is generally difficult and a common simplification comes from assuming spatially dependent global connectivity. The resulting ordinary integrodifferential system is

$$\begin{aligned}\tau_e \frac{\partial r_e}{\partial t} &= -r_e + \Phi_e \left(\tau_e \int_{\Omega} (J_{ee}(|x-y|) r_e(y,t) - J_{ie}(|x-y|) r_i(y,t)) dy + \eta_e + P_e(x,t) \right) \\ \tau_i \frac{\partial r_i}{\partial t} &= -r_i + \Phi_i \left(\tau_i \int_{\Omega} (J_{ei}(|x-y|) r_e(y,t) - J_{ii}(|x-y|) r_i(y,t)) dy + \eta_i + P_i(x,t) \right),\end{aligned}\tag{1.2}$$

These equations differ from the localized excitatory-inhibitory model in that variables are now space dependent, and that the synaptic activation is now represented in terms of an integral where the functions J describe the weight of all synapses from cells a distance $|x - y|$ away. Here the populations are arranged in one dimension on a domain Ω . The simplest one-dimensional topology is given by a ring network, which eliminates boundary conditions. The expansion from the localized E-I network of equations (1.1) to a ring neural field network is schematically represented in Figure 1.1.

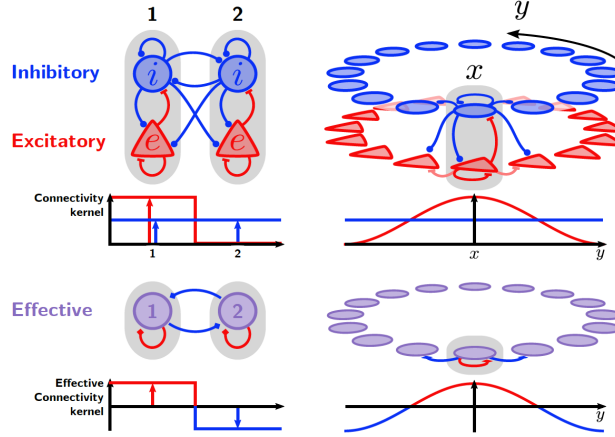


Figure 1.1: Network diagrams representing two cortical columns composed of an excitatory and an inhibitory population of neurons and the continuum extension to a ring network. The connectivity kernels located under each diagram represent the homologous profiles for each system. This Figure has been extracted from [2].

1.2 Linear stability analysis of the effective model

A proper analysis of equations (1.2) is technically impracticable. It's more complicated than the effective one population model, but it is doable. Therefore, with the aim of introducing the bump regime, we study the dynamics of a simplified effective model. By assuming that the excitatory and the inhibitory population of neurons follow the same dynamics we get that

$$\tau_m \frac{\partial r}{\partial t} = -r + \Phi \left(\frac{\tau}{2\pi} \int_{-\pi}^{\pi} J(|x - y|) r(y, t) dy + \xi(x, t) \right), \quad (1.3)$$

where the synaptic connectivity kernel, J , is the combination of the excitatory and inhibitory connection profiles from (1.2), so it represents an effective mixed coupling which may have both positive and negative regions. This consists of the simplest one-dimensional topology, a ring network of length 2π , namely neurons arranged such that

$x \in [-\pi, \pi]$. In the lower graphics from Figure 1.1 in purple we can see a scheme of the effective model. The transition from the discrete two-column model to the continuous ring model is further emphasized by the shape of the connectivity kernels in each case. The connectivity profile in the case of the column model follows a simple cosine function, $J(x) = J_0 + J_1 \cos x$, but a more general connectivity may be applied by considering a general cosine series, asymmetric Fourier series, $J(x) = J_0 + 2 \sum_K J_K \cos(Kx)$, where the choice of the connectivity coefficients follow physiological assumptions.

One very important fact of this networks is that, if we consider the general connectivity profile $J(x) = J_0 + 2 \sum_K J_K \cos(Kx)$, then the model admits two families of spatial solutions. On one hand, at the spatially homogeneous state, or SHS, the activity of the network is flat $r(x, t) = r(t)$ and homogeneous, so the spatial convolution corresponding to the synaptic activation is just $\tau_m J_0 r(t)$. Therefore, from equation (1.3) we have that $\tau \frac{\partial r}{\partial t} = -r + \Phi(I)$, and therefore the firing rate at the spatially homogeneous state is given by $r_0 = \Phi(\tau_m J_0 r_0 + \xi)$, where $r(x, t) = r_0$. By taking the ansatz $r(x, t) = r_0 + \sum_{K=0}^{\infty} \varepsilon_K e^{iKx + \lambda_K t}$, with $\varepsilon_K \ll 1$, we obtain the real-valued eigenvalues $\lambda_k = -\frac{1}{\tau_m} + J_k \Phi_0^{(1)}$, where $\Phi_0^{(1)}$ is the slope of the transfer function evaluated at the fixed point r_0 . Therefore, the stable homogeneous state will destabilize via a pattern-forming (Turing) bifurcation in the neural activity at a critical value of the connectivity mode, that we denote by J_K^c . However, the response of the stable state to a perturbation of wavenumber K will always follow an exponential relaxation with a characteristic time constant proportional to the corresponding value of the connectivity mode, in such a way that the larger the value of the connectivity the longer it takes for the activity to decay to the equilibrium state. The second family of spatial solutions arise at the Turing bifurcation. Above the critical value J_K^c , a spatially inhomogeneous pattern of activity arises consisting of K equidistant bumps of activity. This is the so-called bump state, or BS, which is stable and exhibits the same exponential relaxation process as the homogeneous state. Therefore, key point of the model (1.3) is manifested in the ability of generating bump states and in the different decaying times showed when perturbing the homogeneous state. Further analysis can be followed in [2],[4].

1.3 Spatially inhomogeneous bump state patterns

Spatially dependent synaptic connectivity is known to produce persistent localized regions of higher activity in the network, known as bump states. Several works have exploited the emergence of these spatial patterns in ring networks to model orientation selectivity, such as [1], or other type of feature selectivity such as [5], being these two studies the most important ones. A simple way to understand the mechanism underlying a bump state is to investigate an equivalent situation in a two population effective model, where we have two identical recurrently and cross-coupled populations

with synaptic strengths J_s and J_c , respectively, so

$$\begin{aligned}\tau_m \frac{\partial r_1}{\partial t} &= -r_1 + \Phi(\tau_m J_s r_1 - \tau_m J_c r_2 + \xi_1) \\ \tau_m \frac{\partial r_2}{\partial t} &= -r_2 + \Phi(\tau_m J_s r_2 - \tau_m J_c r_1 + \xi_2)\end{aligned}\tag{1.4}$$

The stability analysis does not differ much from the two population model we studied in the previous section. Again there are no limit cycles and we just have fixed points and the phase portrait can be studied by looking at the intersection of the nullclines, which can be followed in much detail in [2], [6]. As inhibition increases the nullclines twist towards a cubic shape and eventually they cross giving birth to a pair of symmetric stable nodes. Simultaneously the previous stable node loses its stability. This transition corresponds to a Pitchfork bifurcation typical of systems that undergo a symmetry breaking. It is important to remark that models that show this kind of behavior, in which two variables compete for a given state, are often known as winner-takes-all systems and have been used to model two-choice decision making in networks of spiking neurons. The mechanism behind the arousal of the bump state in the effective ring model (1.3) follows this same principle. Similarly, once the cross inhibition is sufficiently high—which is equivalent to increasing the first Fourier coefficient, the stability of the spatially homogeneous state is lost as predicted by the eigenvalues of the linearized system and the bump state emerges.

In [3], the authors proved that under this regime, a ring attractor network could integrate optimally information about oriented stimuli over time. Throughout this thesis we will study the dynamics and how these bump states emerge and how they change over time when forced by external inputs.

2.1 Single population ring model

In the previous chapter we have introduced the main *Neural Field* models, such as the Wilson-Cowan model (1.1). In order to simplify our analysis, we will consider a ring network of a single population, with just one type of connectivity, either excitatory or inhibitory. Hence, in order to set the notation, the simulated ring model follows the expression

$$\tau \frac{\partial r(\theta', t)}{\partial t} = -r(\theta', t) + \Phi \left(\frac{\tau}{2\pi} \int_{-\pi}^{\pi} \omega(\theta - \theta') r(\theta', t) d\theta' + I(\theta, t) \right), \quad (2.1)$$

which describes the dynamics of the firing rate $r = r(\theta, t)$ in a ring network where the spatial variable θ , such that $\theta \in [-\pi, \pi)$, indicates the position in the ring. As we have already mentioned, the spatio-temporal dynamics of the neural activity of the ring is characterized by the particular form of the phenomenological transfer function Φ . The kernel ω represents the coupling among the neurons in the ring network and it can take both positive and negative values. In a ring, any connectivity can be written in terms of the Fourier series

$$\omega(\theta) = \omega_0 + \left(\sum_{k=1}^{\infty} \omega_k e^{ik\theta} + \omega_k^* e^{-ik\theta} \right), \quad (2.2)$$

where we will refer to w_k as the spatial modes of the connectivity. Finally, I corresponds to the spatially structured external input, which can be time dependent, and τ is the neuron's membrane time constant. In Figures 2.1a, 2.1b we can see an scheme of the ring network and the mexican-hat type connectivity.

Following the same linear stability analysis of the homogeneous state with a similar

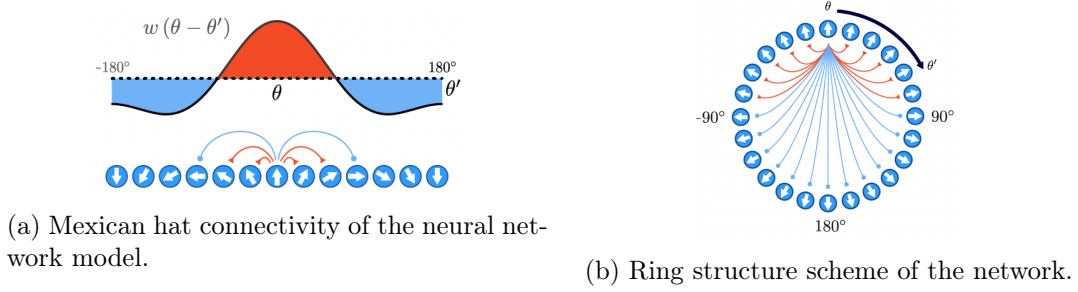


Figure 2.1: Ring network and mexican-hat connectivity schemes.

ansatz, we get that this homogeneous state is $r_0 = \Phi(\tau\omega_0 r_0 + I)$, and that the k -th eigenvalue $\lambda_k = -\frac{1}{\tau} + \omega_k \Phi'_0$, where Φ'_0 is the derivative of the transfer function $\Phi(x)$ evaluated at the fixed point r_0 . Therefore, as we have seen in the introduction, when $\lambda_k = 0$ the system undergoes a Turing instability to a k -bump solution pattern formation, namely the solution for the firing rate equation (2.1) will present k different bumps. In particular, the stable homogeneous state will evolve to a single bump when $\omega_1^T = \frac{1}{\tau\Phi'(\tau\omega_0 r_0 + I)}$ and $\omega_k < \omega_1$ for all $k \neq 1$.

2.2 Derivation of the amplitude equation

The amplitude equation describes the dynamics of the amplitude and the phase of the bump solution in the firing rate of the network near criticality, namely the Turing bifurcation. The importance of this equation lies on the fact that, as stated in [3], it provides an optimal approximation of the firing rate of the ring network and the complex phase of this amplitude can optimally track an stimulus average. Therefore, as our main goal is to study the formation of this bump and how it integrates different Fourier inputs, studying the amplitude equation is the best idea. In order to derive this equation we perform a multiple-scale analysis followed by a perturbation method. As a reference, the derivation is closely related to that of the Stuart-Landau equation, which describes the normal form of a Hopf bifurcation. In fact, the obtained equation is a particular solution of the Ginzburg-Landau equation in which there are no local spatial interactions. More detailed information about this can be found in [9].

In this analysis we will use I , the spatially modulated external input to the network, as the *bifurcation parameter*, as this one has been previously studied in [3]. Other parameters, such as the connectivity profile ω , could also be used to study the bifurcation and that gives rise to the instability that creates the bump in the firing rate.

2.2.1 Spatially homogeneous perturbation

Amplitude equation for a spatially homogeneous perturbation

We start by deriving the amplitude equation for a spatially homogeneous constant perturbation, $I(\theta) = I_{\text{cr}} + \varepsilon^2 I_0$, where $I_{\text{cr}} = I^T$ is the critical value of the external input at which the bump pattern formation takes place. In the following we expand the ring firing rate equation (2.1) in a small enough neighbourhood of the fixed point r_0 . We start by defining the firing rate of the ring network as the sum of small infinitesimal contributions of order ε^n , what can be represented as the infinite series

$$r = r_0 + \sum_{n=1}^{\infty} \varepsilon^n r_n.$$

Furthermore, we can consider the Taylor series of the transfer function $\Phi(x)$ at the critical point $x_0 = \tau\omega_0 r_0 + I_{\text{cr}}$,

$$\Phi(x) = \sum_{n=0}^{\infty} \Phi^{(n)}(x_0)(x-x_0)^n = \Phi(x_0) + \Phi^{(1)}(x_0)(x-x_0) + \frac{1}{2}\Phi^{(2)}(x_0)(x-x_0)^2 + \mathcal{O}(x^3),$$

where $\Phi^{(n)}(x_0)$ denotes the n -th derivative of the transfer function evaluated at the critical point x_0 , in such a way that $x - x_0$, the deviation from the critical fixed point due to the perturbations introduced in the external input and the firing rate, can be expressed as

$$x - x_0 = \frac{\tau}{2\pi} \int_{-\pi}^{\pi} \left(\omega(\theta - \theta') \sum_{n=1}^{\infty} \varepsilon^n r_n \right) d\theta' + \varepsilon^2 I_0. \quad (2.3)$$

We note that, due to the specific choice of the perturbation in the bifurcation parameter, following the same analysis as in [9], it is appropriate to introduce a scaled time T such that $T = \varepsilon^2 t$, and think of the firing rate r as depending both on t , the initial time scale, and T the slower time scale. Both times, the fast and the slow, will be treated as mutually independent and therefore the time differentiation will be made with respect to these two scales, i.e. $\tau \frac{\partial}{\partial t} = \tau \frac{\partial}{\partial t} + \tau \varepsilon^2 \frac{\partial}{\partial T}$, where so as to obtain the last term we have applied the chain rule to the definition of T .

In the following derivations we will work for simplicity with the rescaled quantities $r \rightarrow \tau r$ and $t \rightarrow \frac{t}{\tau}$. By introducing the three previous equations into the firing rate equation of the ring model (2.1), we obtain that

$$\left(\frac{\partial}{\partial t} + \varepsilon^2 \frac{\partial}{\partial T} \right) \sum_{n=0}^{\infty} \varepsilon^n r_n = - \sum_{n=0}^{\infty} \varepsilon^n r_n + \sum_{n=0}^{\infty} \Phi_0^{(n)}(x - x_0)^n, \quad (2.4)$$

where $\Phi_0^{(n)} = \Phi^{(n)}(x_0)$ is the n -th derivative of the transfer function evaluated at the critical point x_0 . The terms corresponding to the critical fixed point vanish on one side

because its temporal dependence is null and on the other side because $r_0 = \Phi_0^{(0)}$, so all sumatories start with the term $n = 1$. In order to simplify the notation, we note that the deviation term $x - x_0$ contains a sum of convolutions, where each term of order n is

$$\begin{aligned} \langle \omega, r_n \rangle_\theta &= \frac{1}{2\pi} \int_{-\pi}^{\pi} \left(\omega_0 + \sum_{k=1}^{\infty} \omega_k e^{ik(\theta-\theta')} + \omega_k^* e^{-ik(\theta-\theta')} \right) \\ &\quad \cdot \left(r_{n0} + \sum_{l=1}^{\infty} r_{nl} e^{il\theta'} + r_{nl}^* e^{-il\theta'} \right) d\theta' = \\ &= \left(\omega_0 r_{n0} + \sum_{k=1}^{\infty} \left(\omega_k r_{nk} e^{ik\theta} + \omega_k^* r_{nk}^* e^{-ik\theta} \right) \right), \end{aligned} \quad (2.5)$$

due to the fact that all periodic terms vanish when integrated in a periodic domain, so we obtain that crossed terms of the kind

$$\int_{-\pi}^{\pi} \omega_k r_{nk} e^{izk\theta'} d\theta' = \int_{-\pi}^{\pi} \omega_k r_{nk} (\cos(zk\theta') + i \sin(zk\theta')) d\theta' = 0, \forall k \in \mathbb{N}, z \in \mathbb{Z} \setminus \{0\},$$

what decouples the Fourier spatial modes as we have seen. Therefore, the deviation from the critical fixed point $x - x_0$ due to the perturbation introduced can be rewritten as

$$x - x_0 = \sum_{n=1}^{\infty} \varepsilon^n \langle \omega, r_n \rangle + \varepsilon^2 I_0.$$

After calculating the Taylor series of the transfer function, which we develop in the equation (A.1) in the Appendix A.1, and collecting terms from equation (2.4) depending on the different orders of ε , we get that

$$(\mathcal{L}_0 + \varepsilon^2 \mathcal{L}_2) \sum_{n=1}^{\infty} \varepsilon^n r_n = \varepsilon^2 \mathcal{N}_2 + \varepsilon^3 \mathcal{N}_3 + \mathcal{O}(\varepsilon^4), \quad (2.6)$$

where we have defined the linear operators of order n as $\mathcal{L}_0 = \tau \frac{\partial}{\partial t} + 1 - \Phi_0^{(1)} \langle \omega, \cdot \rangle_\theta$ and $\mathcal{L}_2 = \frac{\partial}{\partial T}$, and the nonlinear expressions up to third order as

$$\mathcal{N}_2 = \Phi_0^{(1)} I_0 + \frac{\Phi_0^{(2)}}{2} \langle \omega, r_1 \rangle_\theta^2, \quad \mathcal{N}_3 = \Phi_0^{(2)} \langle \omega, r_1 \rangle_\theta (\langle \omega, r_2 \rangle_\theta + I_0) + \frac{\Phi_0^{(3)}}{6} \langle \omega, r_1 \rangle_\theta^3.$$

We note that we have set $\partial_t = 0$, due to the fact that asymptotic expansion is going to be performed in the vicinity of the stationary bifurcation. We could take into account terms of higher orders in ε , but they will not affect the dynamics of the bump. Now, in order to find the temporal evolution of the amplitude of the bump have to solve the differential equation (2.6), what we will do by grouping the different orders of ε . We begin by $\mathcal{O}(\varepsilon)$. In this case, we note that $\mathcal{L}_0 r_1 = r_1 - \Phi_0^{(1)} \langle \omega, r_1 \rangle_\theta = 0$, which is a linear

differential equation on r_1 . If we now express the contribution of first order to the firing rate r_1 in terms of its Fourier series expansion $r_1 = r_{10} + \sum_{k=1}^{\infty} (r_{1k}e^{ik\theta} + r_{1k}^*e^{-ik\theta})$ and use the result from equation (2.5), we get that for the k -th Fourier mode r_{1k} the linear equation becomes $r_{1k}(1 - \omega_k\Phi_0^{(1)}) = 0$. Now, we remember that we had chosen ω_k such that $1 - \omega_k\Phi_0^{(1)} < 0$ if $k \neq 1$ and $1 - \omega_k\Phi_0^{(1)} = 0$ if $k = 1$, so that we had a 1-bump solution. Therefore, all Fourier modes must vanish except for the first one, so that the firing rate contribution at first order is

$$r_1 = A(T)e^{i\theta} + A^*(T)e^{-i\theta}.$$

Additionally, it will be useful to combine the fact that $r_1 = \Phi_0^{(1)}\langle\omega, r_1\rangle_\theta$ with the solution derived so as to obtain

$$\langle\omega, r_1\rangle_\theta = \frac{r_1}{\Phi_0^{(1)}} = \frac{Ae^{i\theta} + A^*e^{-i\theta}}{\Phi_0^{(1)}},$$

and the first two powers

$$\begin{aligned}\langle\omega, r_1\rangle_\theta^2 &= \frac{1}{(\Phi_0^{(1)})^2} \left(A^2e^{2i\theta} + (A^*)^2e^{-2i\theta} + 2|A|^2 \right), \\ \langle\omega, r_1\rangle_\theta^3 &= \frac{1}{(\Phi_0^{(1)})^3} \left(A^3e^{3i\theta} + (A^*)^3e^{-3i\theta} + 3|A|^2Ae^{i\theta} + 3|A|^2A^*e^{-i\theta} \right),\end{aligned}$$

which will be useful for simplifying expressions from contribution of higher orders.

Regarding $\mathcal{O}(\varepsilon^2)$, the terms of second order in ε in equation (2.6), we have that $\mathcal{L}_0r_2 = \mathcal{N}_2$, which if we develop becomes

$$\begin{aligned}\mathcal{L}_0r_2 &= r_2 - \Phi_0^{(1)}\langle\omega, r_2\rangle_\theta = \Phi_0^{(1)}I_0 + \frac{\Phi_0^{(2)}}{2}\langle\omega, r_1\rangle_\theta^2 \\ &= \Phi_0^{(1)}I_0 + \frac{\Phi_0^{(2)}}{2(\Phi_0^{(1)})^2} \left(A^2e^{2i\theta} + (A^*)^2e^{-2i\theta} + 2|A|^2 \right).\end{aligned}$$

If we consider the Fourier series expansion of the contribution of second order to the firing rate, we note that on the term $r_2 - \Phi_0^{(1)}\langle\omega, r_2\rangle_\theta$ there are present all Fourier modes, but on the right hand side term of the equality there are only present modes zero and two, as we can see from the calculations. Hence, all terms in Fourier series expansion different from zero and two must vanish. Therefore, the firing rate at second order in ε has the form $r_2 = r_{20} + (r_{22}e^{2i\theta} + r_{22}^*e^{-2i\theta})$. Now, splitting the equation into the two

different modes we have that

$$r_{20} - \Phi_0^{(1)} \omega_0 r_{20} = \Phi_0^{(1)} I_0 + \frac{\Phi_0^{(2)}}{2 \left(\Phi_0^{(1)} \right)^2} 2|A|^2, \quad r_{22} - \Phi_0^{(1)} \omega_2 r_{22} = \frac{\Phi_0^{(2)}}{2 \left(\Phi_0^{(1)} \right)^2} A^2,$$

so that we finally obtain that the zeroth and second Fourier spatial order terms of r_2 are

$$r_{20} = \frac{\Phi_0^{(1)}}{1 - \omega_0 \Phi_0^{(1)}} I_0 + \frac{\Phi_0^{(2)}}{\left(\Phi_0^{(1)} \right)^2 \left(1 - \omega_0 \Phi_0^{(1)} \right)} |A|^2, \quad r_{22} = \frac{\Phi_0^{(2)}}{2 \left(\Phi_0^{(1)} \right)^2 \left(1 - \omega_2 \Phi_0^{(1)} \right)} A^2.$$

Finally, the terms of third order in ε contain the evolution of the amplitude A of the bump through the derivative of r_1 with respect to the slow time T . So as to find this expression, we recall that the $\mathcal{O}(\varepsilon^3)$ terms in equation (2.6) lead to an expression of the form

$$\mathcal{L}_0 r_3 + \mathcal{L}_2 r_1 = r_3 - \Phi_0^{(1)} \langle \omega, r_3 \rangle_\theta + \frac{\partial r_1}{\partial T} = \Phi_0^{(2)} \langle \omega, r_1 \rangle_\theta (\langle \omega, r_2 \rangle_\theta + I_0) + \frac{\Phi_0^{(3)}}{6} \langle \omega, r_1 \rangle_\theta^2.$$

If we now substitute the previous expressions derived for the different convolutions, we have that

$$r_3 - \Phi_0^{(1)} \langle \omega, r_3 \rangle_\theta + \frac{\partial r_1}{\partial T} = \Phi_0^{(2)} \frac{A}{\Phi_0^{(1)}} (\omega_0 r_{20} + \omega_2 r_{22} + I_0) + \frac{\Phi_0^{(3)}}{6 \left(\Phi_0^{(1)} \right)^3} (A^3 + 3|A|^2 A),$$

where we have expressed all terms of the form $A^n e^{in\theta} + (A^*)^n e^{-in\theta}$ as A^n for the ease of reading. At this point of the calculations it is useful to compute the inner product Ar_{22} , which is equivalent to AA^2 , and we obtain that

$$\left(Ae^{i\theta} + A^* e^{-i\theta} \right) \left(A^2 e^{2i\theta} + (A^*)^2 e^{-2i\theta} \right) = \left(A^3 e^{3i\theta} + (A^*)^3 e^{-3i\theta} \right) + |A|^2 (Ae^{i\theta} + A^* e^{-i\theta}).$$

Now, we note that, while the left hand side of the equality is a combination of all Fourier modes of r_3 and r_1 , the right hand side of the equation is a combination of terms of first and third order, terms that go as $e^{i\theta}$ and $e^{3i\theta}$. Therefore, performing in a similar manner as with the previous orders in ε and splitting into the different Fourier modes we have that

$$\begin{aligned} r_{31} \left(1 - \omega_1 \Phi_0^{(1)} \right) + \frac{\partial A}{\partial T} &= \frac{\partial A}{\partial T} = \frac{\Phi_0^{(2)}}{\Phi_0^{(1)}} \left(\frac{\omega_0 \Phi_0^{(1)}}{1 - \omega_0 \Phi_0^{(1)}} I_0 + I_0 \right) A + \\ &+ \left(\frac{\Phi_0^{(2)}}{\Phi_0^{(1)}} \left(\frac{|A|^2 A \omega_0 \Phi_0^{(2)}}{\left(\Phi_0^{(1)} \right)^2 \left(1 - \omega_0 \Phi_0^{(1)} \right)} + \frac{|A|^2 A \omega_2 \Phi_0^{(2)}}{2 \left(\Phi_0^{(1)} \right)^2 \left(1 - \omega_2 \Phi_0^{(1)} \right)} \right) + \frac{|A|^2 A \Phi_0^{(3)}}{2 \left(\Phi_0^{(1)} \right)^3} \right), \end{aligned} \quad (2.7)$$

where we have used the hypothesis $1 - \omega_1 \Phi_0^{(1)} = 0$ due to the fact that we only want the first Fourier mode to destabilize, while for the third mode we have that

$$r_{33} \left(1 - \omega_3 \Phi_0^{(1)}\right) = \left(\frac{\Phi_0^{(2)}}{\Phi_0^{(1)}} \frac{\omega_2 \Phi_0^{(2)}}{2 \left(\Phi_0^{(1)}\right)^2 \left(1 - \omega_2 \Phi_0^{(1)}\right)} + \frac{\Phi_0^{(3)}}{6 \left(\Phi_0^{(1)}\right)^3} \right) A^3.$$

Finally, simplifying terms in equation (2.7) and recovering the dimensions, $T \sim \frac{1}{\tau}$, $A \sim \tau$ and $\Phi_0^{(n)} \sim \frac{1}{\tau}$, we have that

$$\tau \frac{\partial A}{\partial T} = \frac{\Phi_0^{(2)} I_0 A}{\Phi_0^{(1)} \left(1 - \tau \omega_0 \Phi_0^{(1)}\right)} + \frac{\left(\Phi_0^{(2)}\right)^2}{\left(\Phi_0^{(1)}\right)^3} \left(\frac{\tau \omega_0 |A|^2 A}{1 - \tau \omega_0 \Phi_0^{(1)}} + \frac{\tau \omega_2 |A|^2 A}{2 \left(1 - \tau \omega_2 \Phi_0^{(1)}\right)} \right) + \frac{\tau^3 \Phi_0^{(3)} |A|^2 A}{2 \left(\Phi_0^{(1)}\right)^3}, \quad (2.8)$$

which is the amplitude equation of the bump for a spatially homogeneous perturbation.

Dynamics of the amplitude equation

The complex-valued amplitude equation (2.8) can be written in polar notation if we denote the amplitude of the bump as $A = R e^{-i\psi}$, where R and ψ are respectively the real-valued amplitude and the phase of the bump. The equation is then

$$\tau e^{-i\psi} \frac{\partial R}{\partial t} - i \tau R e^{-i\psi} \frac{\partial \psi}{\partial t} = \alpha R e^{-i\psi} + \beta R^3 e^{-i\psi}, \quad (2.9)$$

where

$$\alpha = \frac{\Phi_0^{(2)}}{\Phi_0^{(1)} \left(1 - \tau \omega_0 \Phi_0^{(1)}\right)} I_0, \beta = \frac{\left(\Phi_0^{(2)}\right)^2}{\left(\Phi_0^{(1)}\right)^3} \left(\frac{\tau \omega_0}{1 - \tau \omega_0 \Phi_0^{(1)}} + \frac{\tau \omega_2}{2 \left(1 - \tau \omega_2 \Phi_0^{(1)}\right)} \right) + \frac{\tau^3 \Phi_0^{(3)}}{2 \left(\Phi_0^{(1)}\right)^3}.$$

Splitting the above equation in its real and imaginary parts leads to a system of two coupled ordinary differential equations, that is

$$\begin{aligned} \tau \frac{\partial R}{\partial t} &= \alpha R + \beta R^3, \\ \tau R \frac{\partial \psi}{\partial t} &= 0. \end{aligned} \quad (2.10)$$

Therefore, we note that when the input is spatially homogeneous, the amplitude of the bump changes but the phase remains constant. In fact, from [3] we know that this is in fact a gradient system that can be derived from a potential. Hence, in the absence of stimulus input, the potential resembles a juice-squeezer-shaped surface with an unstable fixed point at the center corresponding to a bump with zero amplitude ($R = 0$).

2.2.2 Spatially inhomogeneous perturbation

In order to model an orientation-related stimuli, we now set the input I to be spatially modulated. The general form of such perturbation from the critical fixed point I_{cr} can be written, in terms of its Fourier series, as

$$I(\theta) = I_{\text{cr}} + I_0 + \sum_{k=1}^{\infty} \left(I_k e^{ik\theta} + I_k^* e^{-ik\theta} \right) = I_{\text{cr}} + I_0 + 2 \sum_{k=1}^{\infty} \bar{I}_k \cos(k(\theta - \theta^*)),$$

where $I_k = \bar{I}_k e^{-ik\theta^*}$ also live in the Fourier space. However, if we want to model the stimuli used in many behavioural tasks we can consider only the first Fourier mode, in addition to the mean input, namely $I(\theta) = I_{\text{cr}} + I_0 + (I_1 e^{i\theta} + I_1^* e^{-i\theta})$. We note that, as our goal is to excite those neurons whose preferred orientation is closer to the direction of the stimulus and inhibit the rest, the first Fourier mode of the input should be the strongest mode of the input signal.

In general, we can consider inputs of higher order Fourier terms as well. In particular, this is interesting because we will consider such signals as decision or urgency signals that can force the network to make a categorical decision, such as between a clockwise (CW) or counterclockwise (CCW) movement of a stimulus. The goal of such inputs is to excite the neurons of the ring with positive preferred orientations if the stimulus was clockwise or to activate the neurons with negative preferred orientation if the stimulus was counterclockwise. With this purpose, we will study how the ring network integrates this kind of higher order stimulus by deriving the amplitude equation for a modulated input to the network of order one to four.

Amplitude equation for a First order Fourier mode input

We follow the same procedure as in the previous sections, but in this case expanding the ring equation (2.1) over the modulated input $I(\theta) = I_{\text{cr}} + \varepsilon^2 I_0 + 2\varepsilon^3 \bar{I}_1 \cos(\theta - \theta^*)$, where θ^* is a fixed direction of a stimulus. After calculating the Taylor series expansion of the transfer function in the equation (A.2) in the Appendix A.1, we note that the ring equation can be again written in a more compact way as

$$(\mathcal{L}_0 + \varepsilon^2 \mathcal{L}_2) \sum_{n=1}^{\infty} \varepsilon^n r_n = \varepsilon^2 \mathcal{N}_2 + \varepsilon^3 \mathcal{N}_3 + \mathcal{O}(\varepsilon^4), \quad (2.11)$$

where \mathcal{L}_0 , \mathcal{L}_2 and \mathcal{N}_2 are the same operators as the ones from equation (2.6) and the only change applies to the nonlinear operator of third order, which in this case becomes

$$\mathcal{N}_3 = \Phi_0^{(1)} 2\bar{I}_1 \cos(\theta - \theta^*) + \Phi_0^{(2)} \langle \omega, r_1 \rangle_{\theta} (\langle \omega, r_2 \rangle_{\theta} + I_0) + \frac{\Phi_0^{(3)}}{6} \langle \omega, r_1 \rangle_{\theta}^3.$$

Therefore, the solutions to first and second order are identical, as the linear systems to solve do not change. The solution to third order changes slightly, but is derived in a similar way. Again, the terms of third order in ε finally contain the evolution of the amplitude A through the derivative of r_1 with respect to the slow time T . So as to find this expression, we recall that the $\mathcal{O}(\varepsilon^3)$ terms in equation (2.11) lead to the expression

$$r_3 - \Phi_0^{(1)} \langle \omega, r_3 \rangle_\theta + \frac{\partial r_1}{\partial T} = \Phi_0^{(1)} I_1 e^{i(\theta - \theta^*)} + \Phi_0^{(2)} \langle \omega, r_1 \rangle_\theta (\langle \omega, r_2 \rangle_\theta + I_0) + \frac{\Phi_0^{(3)}}{6} \langle \omega, r_1 \rangle_\theta^2,$$

where we have expressed the modulated first Fourier order input in its complex form. Similarly to what we did with the homogeneous input, by substituting the known terms we get that

$$r_3 - \Phi_0^{(1)} \langle \omega, r_3 \rangle_\theta + \frac{\partial r_1}{\partial T} = \Phi_0^{(1)} I_1 e^{i(\theta - \theta^*)} + \Phi_0^{(2)} \frac{A}{\Phi_0^{(1)}} (\omega_0 r_{20} + \omega_2 r_{22} + I_0) + \frac{\Phi_0^{(3)} (A^3 + 3|A|^2 A)}{6 (\Phi_0^{(1)})^3},$$

where we have expressed all terms of the form $A^n e^{in\theta} + (A^*)^n e^{-in\theta}$ as A^n for the ease of reading. We can see that this expression is very similar to the one from the homogeneous input, so again we note that the right hand side of the equation is a combination of terms of first and third order, terms that go as $e^{i\theta}$ and $e^{3i\theta}$. Therefore, performing in a similar manner as with the previous orders in ε and splitting into the different modes we have for the first mode, which is the only we will calculate as it contains the dynamics of the amplitude, that

$$\begin{aligned} \frac{\partial A}{\partial T} = & \Phi_0^{(1)} I_1 e^{-i\theta^*} + \frac{\Phi_0^{(2)}}{\Phi_0^{(1)}} \left(\frac{\omega_0 \Phi_0^{(1)}}{1 - \omega_0 \Phi_0^{(1)}} I_0 + I_0 \right) A + \\ & + \left(\frac{\Phi_0^{(2)}}{\Phi_0^{(1)}} \left(\frac{|A|^2 A \omega_0 \Phi_0^{(2)}}{(\Phi_0^{(1)})^2 (1 - \omega_0 \Phi_0^{(1)})} + \frac{|A|^2 A \omega_2 \Phi_0^{(2)}}{2 (\Phi_0^{(1)})^2 (1 - \omega_2 \Phi_0^{(1)})} \right) + \frac{|A|^2 A \Phi_0^{(3)}}{2 (\Phi_0^{(1)})^3} \right). \end{aligned} \quad (2.12)$$

Finally, simplifying terms in the equation (2.12) and recovering the dimensions, $T \sim \frac{1}{\tau}$, $A \sim \tau$ and $\Phi_0^{(n)} \sim \frac{1}{\tau}$, we have that

$$\begin{aligned} \tau \frac{\partial A}{\partial T} = & \Phi_0^{(1)} I_1 e^{-i\theta^*} + \frac{\Phi_0^{(2)} I_0 A}{\Phi_0^{(1)} (1 - \tau \omega_0 \Phi_0^{(1)})} + \frac{(\Phi_0^{(2)})^2}{(\Phi_0^{(1)})^3} \left(\frac{\tau \omega_0 |A|^2 A}{1 - \tau \omega_0 \Phi_0^{(1)}} + \frac{\tau \omega_2 |A|^2 A}{2 (1 - \tau \omega_2 \Phi_0^{(1)})} \right) \\ & + \frac{\tau^3 \Phi_0^{(3)} |A|^2 A}{2 (\Phi_0^{(1)})^3}, \end{aligned} \quad (2.13)$$

that is the amplitude equation of the bump for a spatially inhomogeneous perturbation of first Fourier order, namely, when the stimulus is present.

Dynamics of the amplitude equation

As we have performed previously, the complex-valued amplitude equation (2.13) can be written in polar notation if we denote the amplitude of the bump as $A = Re^{-i\psi}$, where R and ψ are respectively the real value amplitude and the phase of the bump. The equation is then

$$\tau e^{-i\psi} \frac{\partial R}{\partial t} - i\tau R e^{-i\psi} \frac{\partial \psi}{\partial t} = \tilde{I}_1 e^{-i\theta^*} + \alpha R e^{-i\psi} + \beta R^3 e^{-i\psi},$$

where α, β are defined as previously and $\tilde{I}_1 = \Phi_0^{(1)} I_1$. Splitting the equation in its real and imaginary parts leads again to a system of two coupled ordinary differential equations, that is

$$\begin{aligned} \tau \frac{\partial R}{\partial t} &= \tilde{I}_1 \cos(\psi - \theta^*) + \alpha R + \beta R^3, \\ \tau \frac{\partial \psi}{\partial t} &= -\frac{\tilde{I}_1}{R} \sin(\psi - \theta^*), \end{aligned}$$

As with the homogeneous input, this dynamical system is in fact a gradient system that can be obtained from a potential, as stated in [3]. There, the authors realized that when presenting a stimulus to the network the radial symmetry of the potential breaks and a deeper region arises at the location of the stimulus θ^* . If the particle has already reached the stable circular manifold at the bottom of the potential, the stimulus will force it to move towards this deeper state along the manifold. In terms of the activity of the network, this corresponds to a movement of the bump towards θ^* , accompanied by slight changes in the bump's amplitude, as we can see from the dynamical system.

Amplitude equation for a Second order Fourier mode input

We begin now to study how does the ring network integrate higher order Fourier inputs, which can be considered as decision or urgency signals so as to force the network make a decision. The first case that we will consider is the spatial modulated input of wavenumber $k = 2$ and a fixed orientation of $\theta^* = \frac{\pi}{2}$. Therefore, in this case we will expand the ring equation (2.1) over the modulated input $I(\theta) = I_{\text{cr}} + \varepsilon^2 I_0 + \varepsilon^2 2\bar{I}_2 \cos(2(\theta - \frac{\pi}{2}))$. This change in the order of ε of the perturbation term $2\bar{I}_2 \cos(2(\theta - \frac{\pi}{2}))$ is due to the fact that other orders decouple the effect of the perturbation from the dynamics of the amplitude of the bump, what we want to avoid. After calculating the Taylor series expansion of the transfer function in equation (A.3) in the Appendix A.1, we note that

the ring equation can be written in a more compact way as

$$(\mathcal{L}_0 + \varepsilon^2 \mathcal{L}_2) \sum_{n=1}^{\infty} \varepsilon^n r_n = \varepsilon^2 \mathcal{N}_2 + \varepsilon^3 \mathcal{N}_3 + \mathcal{O}(\varepsilon^4), \quad (2.14)$$

where $\mathcal{L}_0, \mathcal{L}_2$ are the same linear operators defined in equation (2.6) and the nonlinear operators change to be

$$\mathcal{N}_2 = \Phi_0^{(1)} \left(I_0 + 2\bar{I}_2 \cos \left(2 \left(\theta - \frac{\pi}{2} \right) \right) \right) + \frac{\Phi_0^{(2)}}{2} \langle \omega, r_1 \rangle_{\theta}^2,$$

and

$$\mathcal{N}_3 = \Phi_0^{(2)} \langle \omega, r_1 \rangle_{\theta} \left(\langle \omega, r_2 \rangle_{\theta} + I_0 + 2\bar{I}_2 \cos \left(2 \left(\theta - \frac{\pi}{2} \right) \right) \right) + \frac{\Phi_0^{(3)}}{6} \langle \omega, r_1 \rangle_{\theta}^3.$$

We note that the solution of first order r_1 does not change, due to the fact that the system $\mathcal{L}_0 r_1 = 0$ does not change. However, the solution of second order does change due to the change in the nonlinear operator \mathcal{N}_2 . In this case, the terms of second order $\mathcal{O}(\varepsilon^2)$ lead to an expression of the form

$$\mathcal{L}_0 r_2 = r_2 - \Phi_0^{(1)} \langle \omega, r_2 \rangle_{\theta} = \Phi_0^{(1)} \left(I_0 + I_2 e^{2i(\theta - \frac{\pi}{2})} \right) + \frac{\Phi_0^{(2)}}{2} \langle \omega, r_1 \rangle_{\theta}^2,$$

where we have expressed the decision signal in its complex form and avoid writing the complex conjugate terms, as they will not affect. Again, we note that the right hand side of the equality is a combination of terms of zeroth and second order, while on the left hand side all the equality all modes are present. Therefore, all modes must vanish except for the zeroth and second. Splitting the equation into this two modes which do not vanish we have that

$$r_{20} - \Phi_0^{(1)} \omega_0 r_{20} = \Phi_0^{(1)} I_0 + \frac{\Phi_0^{(2)}}{\left(\Phi_0^{(1)} \right)^2} |A|^2, \quad r_{22} - \Phi_0^{(1)} \omega_2 r_{22} = \Phi_0^{(1)} I_2 e^{-2i\frac{\pi}{2}} + \frac{\Phi_0^{(2)}}{2 \left(\Phi_0^{(1)} \right)^2} A^2.$$

We note that r_{20} does not change, so we will focus on calculating the second Fourier term of the contribution of second order to the firing rate r_{22} , which is

$$r_{22} = \frac{\Phi_0^{(1)}}{1 - \Phi_0^{(1)} \omega_2} I_2 e^{-2i\frac{\pi}{2}} + \frac{\Phi_0^{(2)}}{2 \left(\Phi_0^{(1)} \right)^2 \left(1 - \Phi_0^{(1)} \omega_2 \right)} A^2.$$

As it has been happening so far, the terms of third order in ε , specifically the first Fourier term of the contribution to third order to the firing rate, finally contain the temporal dynamics of the amplitude A of the bump through the derivative of r_1 with

respect to the slow time T . So as to find this expression, we recall that the $\mathcal{O}(\varepsilon^3)$ terms of (2.14) satisfy the linear system $\mathcal{L}_0 r_3 + \mathcal{L}_2 r_1 = \mathcal{N}_3$, that can be expanded to be

$$\begin{aligned} r_3 - \Phi_0^{(1)} \langle \omega, r_3 \rangle_\theta + \frac{\partial r_1}{\partial T} &= \Phi_0^{(2)} \langle \omega, r_1 \rangle_\theta \left(\langle \omega, r_2 \rangle_\theta + I_0 + 2\bar{I}_2 \cos \left(2 \left(\theta - \frac{\pi}{2} \right) \right) \right) + \frac{\Phi_0^{(3)}}{6} \langle \omega, r_1 \rangle^3 \\ &= \Phi_0^{(2)} \langle \omega, r_1 \rangle_\theta \left(\langle \omega, r_2 \rangle_\theta + I_0 + 2I_2 e^{2i(\theta - \frac{\pi}{2})} \right) + \frac{\Phi_0^{(3)}}{6} \langle \omega, r_1 \rangle^3, \end{aligned}$$

where in the last expression we have written the second order Fourier input in its complex form and we have avoided writing the complex conjugate term, as it doesn't affect. The right hand side of the equality is a combination of terms of first and third order, and therefore all modes on the left hand side of the equality different must vanish. Substituting and splitting the equation into this two different spatial terms, and focusing only on the first Fourier mode contribution, as it contains the dynamics of the amplitude equation, we have that

$$\begin{aligned} r_{31} \left(1 - \omega_1 \Phi_0^{(1)} \right) + \frac{\partial A}{\partial T} &= \left(\frac{\Phi_0^{(2)}}{\Phi_0^{(1)}} \frac{\omega_2 \Phi_0^{(1)}}{1 - \Phi_0^{(1)} \omega_2} + \frac{\Phi_0^{(2)}}{\Phi_0^{(1)}} \right) I_2 e^{-2i\frac{\pi}{2}} A^* \\ &+ \frac{\Phi_0^{(2)}}{\Phi_0^{(1)}} \left(\frac{\omega_0 \Phi_0^{(1)}}{1 - \omega_0 \Phi_0^{(1)}} I_0 + I_0 \right) A \\ &+ \left(\frac{\Phi_0^{(2)}}{\Phi_0^{(1)}} \left(\frac{\omega_0 \Phi_0^{(2)}}{(\Phi_0^{(1)})^2 (1 - \omega_0 \Phi_0^{(1)})} + \frac{\omega_2 \Phi_0^{(2)}}{2 (\Phi_0^{(1)})^2 (1 - \omega_2 \Phi_0^{(1)})} \right) + \frac{\Phi_0^{(3)}}{2 (\Phi_0^{(1)})^3} \right) |A|^2 A, \end{aligned}$$

Therefore, simplifying from the expression of the first spatial Fourier mode, using the hypothesis that $1 - \omega_1 \Phi_0^{(1)} = 0$ and recovering the dimensions we have that

$$\begin{aligned} \tau \frac{\partial A}{\partial T} &= \left(\frac{\tau^2 \Phi_0^{(2)}}{\tau \Phi_0^{(1)}} \frac{1}{1 - \tau \Phi_0^{(1)} \omega_2} \right) I_2 e^{-2i\frac{\pi}{2}} A^* + \frac{\Phi_0^{(2)} I_0 A}{\Phi_0^{(1)} (1 - \tau \omega_0 \Phi_0^{(1)})} \\ &+ \frac{(\Phi_0^{(2)})^2}{(\Phi_0^{(1)})^3} \left(\frac{\tau \omega_0 |A|^2 A}{1 - \tau \omega_0 \Phi_0^{(1)}} + \frac{\tau \omega_2 |A|^2 A}{2 (1 - \tau \omega_2 \Phi_0^{(1)})} \right) + \frac{\tau^3 \Phi_0^{(3)} |A|^2 A}{2 (\Phi_0^{(1)})^3}, \end{aligned} \quad (2.15)$$

which is the equation that describes the dynamics of the amplitude of the bump after the integration of a spatially modulated input of second Fourier order.

Dynamics of the amplitude equation

As we have performed previously, the complex-valued amplitude equation (2.15) can be written in polar notation if we denote the amplitude of the bump as $A = R e^{-i\psi}$, where R and ψ are respectively the real value amplitude and the phase of the bump.

The equation is then

$$\tau e^{-i\psi} \frac{\partial R}{\partial t} - i\tau R e^{-i\psi} \frac{\partial \psi}{\partial t} = \gamma \tilde{I}_2 R e^{i(\psi-\pi)} + \alpha R e^{-i\psi} + \beta R^3 e^{-i\psi},$$

which is equivalent to

$$\tau \frac{\partial R}{\partial t} - i\tau R \frac{\partial \psi}{\partial t} = \gamma \tilde{I}_2 R e^{2i(\psi-\frac{\pi}{2})} + \alpha R + \beta R^3,$$

where α, β are defined as previously and $\tilde{I}_2 = \Phi_0^{(1)} I_2$. Splitting the equation in its real and imaginary parts leads again to a system of two coupled ODEs, that is

$$\begin{aligned} \tau \frac{\partial R}{\partial t} &= \gamma \tilde{I}_2 \cos\left(2\left(\psi - \frac{\pi}{2}\right)\right) R + \alpha R + \beta R^3, \\ \tau \frac{\partial \psi}{\partial t} &= -\gamma \tilde{I}_2 \sin\left(2\left(\psi - \frac{\pi}{2}\right)\right), \end{aligned}$$

after multiplying all terms of the equation by $e^{i\psi}$. In this case, it is remarkable that this dynamical system is uncoupled, as the phase of the bump, for example, does not depend anymore on the amplitude of the bump.

Amplitude equation for a Third order Fourier mode input

Now we are going to perform the same analysis for a third order Fourier input, namely a spatially modulated input signal with wavenumber $k = 3$. The main difference with respect to the previous input is the fact that the fixed points are closer to the reference. Instead of having $\pm \frac{\pi}{2}$ as fix points of the phase of the bump, we will see that in this case these are $\pm \frac{\pi}{3}$, what will be very helpful later so as to fit more accurately the psychophysical data. In this case, we will expand the ring equation (2.1) over the input $I(\theta) = I_{\text{cr}} + \varepsilon^2 I_0 + \varepsilon 2\bar{I}_3 \cos\left(3\left(\theta - \frac{\pi}{3}\right)\right)$. Again, the change in the order of the perturbation is done only with the purpose of managing to get the effect of the stimulus input in the dynamics of the amplitude of the bump. After calculating the Taylor series expansion of the transfer function in the equation (A.4) in the Appendix A.1, we note that the ring equation (2.1) can be written in a more compact way as

$$(\mathcal{L}_0 + \varepsilon^2 \mathcal{L}_2) \sum_{n=1}^{\infty} \varepsilon^n r_n = \varepsilon 2\bar{I}_3 \cos\left(3\left(\theta - \frac{\pi}{3}\right)\right) + \varepsilon^2 \mathcal{N}_2 + \varepsilon^3 \mathcal{N}_3 + \mathcal{O}(\varepsilon^4), \quad (2.16)$$

where $\mathcal{L}_0, \mathcal{L}_2$ are the same linear operators defined in equation (2.6) and the nonlinear operators are

$$\mathcal{N}_2 = \Phi_0^{(1)} I_0 + \frac{\Phi_0^{(2)}}{2} \left(\langle \omega, r_1 \rangle_{\theta} + 2\bar{I}_3 \cos\left(3\left(\theta - \frac{\pi}{3}\right)\right) \right)^2,$$

and

$$\mathcal{N}_3 = \Phi_0^{(2)} \left(\langle \omega, r_1 \rangle_\theta + 2\bar{I}_3 \cos \left(3 \left(\theta - \frac{\pi}{3} \right) \right) \right) (\langle \omega, r_2 \rangle_\theta + I_0)$$

The solution of first order r_1 in this case does change because of the appearance of the term $\varepsilon 2\bar{I}_3 \cos \left(3 \left(\theta - \frac{\pi}{3} \right) \right)$. Now, the linear system to solve is $\mathcal{L}_0 r_1 = \varepsilon 2\bar{I}_3 \cos \left(3 \left(\theta - \frac{\pi}{3} \right) \right)$, so it is clear that apart from the first order term that appears in all derivations, $r_{11} = A e^{i\theta}$, there will also be a third order mode in its Fourier series expansion, $r_{13} = \frac{A I_3}{1 - \omega_3 \Phi_0^{(1)}} e^{-3i\frac{\pi}{3}}$.

Regarding the second order terms of the equality $\mathcal{O}(\varepsilon^2)$ from (2.16), we have that $\mathcal{L}_0 r_2 = \mathcal{N}_2$, which if we develop becomes

$$r_2 - \Phi_0^{(1)} \langle \omega, r_2 \rangle_\theta = \Phi_0^{(1)} I_0 + \frac{\Phi_0^{(2)}}{2} \left(\langle \omega, r_1 \rangle_\theta + 2\bar{I}_3 \cos \left(3 \left(\theta - \frac{\pi}{3} \right) \right) \right)^2.$$

In this case, following the development of the quadratic expression in the Appendix A.1, one can appreciate that the right hand side term of the equality is a combination of terms of order zero, two, four and six, where in particular the term of second order is

$$r_{22} = \frac{1}{1 - \omega_2 \Phi_0^{(1)}} \left(2\omega_1^2 r_{11}^2 + 2\omega_1^* r_{11}^* \omega_3 r_{13} + 2\omega_1^* r_{11}^* I_3 e^{-3i\frac{\pi}{3}} \right).$$

If we now focus in the solution to third order, in other words the terms $\mathcal{O}(\varepsilon^3)$ of (2.16), we have that the linear system to solve is $\mathcal{L}_0 r_3 + \mathcal{L}_2 r_1 = \mathcal{N}_3$, which if we expand becomes

$$r_3 - \Phi_0^{(1)} \langle \omega, r_3 \rangle_\theta + \frac{\partial r_1}{\partial T} = \Phi_0^{(2)} \left(\langle \omega, r_1 \rangle_\theta + 2\bar{I}_3 \cos \left(3 \left(\theta - \frac{\pi}{3} \right) \right) \right) (\langle \omega, r_2 \rangle_\theta + I_0).$$

So as to ease the reading, we will again only focus on looking for the first Fourier spatial mode of the term with contribution of third order of the firing rate, which contains the evolution of the amplitude A of the bump through the derivative of r_1 with respect to the slow time T . In this case, both terms $\Phi_0^{(2)} \langle \omega, r_1 \rangle_\theta (\langle \omega, r_2 \rangle_\theta + I_0)$ and $\Phi_0^{(2)} 2\bar{I}_3 \cos \left(3 \left(\theta - \frac{\pi}{3} \right) \right) (\langle \omega, r_2 \rangle_\theta + I_0)$ contain terms of first order. Hence, the first mode of the contribution of third order to the firing rate r_3 satisfies that

$$\begin{aligned} r_{31}(1 - \omega_1 \Phi_0^{(1)}) + \frac{\partial A}{\partial T} &= \Phi_0^{(2)} \left(\omega_3 r_{13} + I_3 e^{-3i\frac{\pi}{3}} \right) \omega_2^* r_{12}^* + \Phi_0^{(2)} I_0 \omega_1 r_{11} = \\ &\Phi_0^{(2)} \omega_3 r_{13} \left(2\omega_2^* (\omega_1^*)^2 (r_{11}^*)^2 + 2\omega_2^* \omega_1 r_{11} \omega_3^* r_{13}^* + 2\omega_2^* \omega_1 r_{11} I_3^* e^{3i\frac{\pi}{3}} \right) \\ &\Phi_0^{(2)} I_0 \omega_1 r_{11} + \\ &\Phi_0^{(2)} I_3 e^{-3i\frac{\pi}{3}} \left(2\omega_2^* (\omega_1^*)^2 (r_{11}^*)^2 + 2\omega_2^* \omega_1 r_{11} \omega_3^* r_{13}^* + 2\omega_2^* \omega_1 r_{11} I_3^* e^{3i\frac{\pi}{3}} \right) \end{aligned} \quad (2.17)$$

Hence, using the fact that $1 - \omega_1 \Phi_0^{(1)} = 0$, we obtain that the dynamics of the amplitude

of the bump is given by the expression

$$\begin{aligned} \frac{\partial A}{\partial T} = & \Phi_0^{(2)} \omega_3 r_{13} \left(2\omega_2^* (\omega_1^*)^2 (r_{11}^*)^2 + 2\omega_2^* \omega_1 r_{11} \omega_3^* r_{13}^* + 2\omega_2^* \omega_1 r_{11} I_3^* e^{3i\frac{\pi}{3}} \right) + \Phi_0^{(2)} I_0 \omega_1 r_{11} + \\ & \Phi_0^{(2)} I_3 e^{-3i\frac{\pi}{3}} \left(2\omega_2^* (\omega_1^*)^2 (r_{11}^*)^2 + 2\omega_2^* \omega_1 r_{11} \omega_3^* r_{13}^* + 2\omega_2^* \omega_1 r_{11} I_3^* e^{3i\frac{\pi}{3}} \right), \end{aligned}$$

and by replacing all terms and setting $\tau = 1$ so that no reescalating is necessary, we get that

$$\begin{aligned} \frac{\partial A}{\partial T} = & \Phi_0^{(2)} \left(\frac{2\omega_3 \omega_2^* (\omega_1^*)^2 I_3 e^{-3i\frac{\pi}{3}}}{(1 - \omega_2 \Phi_0^{(1)})} + \frac{2|\omega_3|^2 \omega_2^* \omega_1 |I_3|^2}{(1 - \omega_2 \Phi_0^{(1)}) (1 - \omega_3^* \Phi_0^{(1)})} \right) |A|^2 A^* + \\ & \Phi_0^{(2)} \left(\frac{2\omega_3 \omega_2^* (\omega_1^*)^2 |I_3|^2}{(1 - \omega_2 \Phi_0^{(1)})} \right) A^2 + \Phi_0^{(2)} \left(\frac{2\omega_2^* (\omega_1^*)^2 I_3 e^{-3i\frac{\pi}{3}}}{(1 - \omega_2 \Phi_0^{(1)})} \right) (A^*)^2 + \\ & \Phi_0^{(2)} \left(\frac{2\omega_2^* \omega_1 |I_3|^2}{(1 - \omega_2 \Phi_0^{(1)}) (1 - \omega_3^* \Phi_0^{(1)})} \right) |A|^2 + \Phi_0^{(2)} (I_0 \omega_1 + 2\omega_2^* \omega_1 |I_3|^2) A \\ = & \alpha_1 I_3 e^{-3i\frac{\pi}{3}} |A|^2 A^* + \alpha_2 |A|^2 A^* + \beta A^2 + \gamma I_3 e^{-3i\frac{\pi}{3}} (A^*)^2 + \delta |A|^2 + \epsilon A \end{aligned} \quad (2.18)$$

Dynamics of the amplitude equation

The amplitude equation (2.18) can be rewritten in polar notation by substituting again $A = Re^{-i\psi}$, so we obtain that

$$\tau e^{-i\psi} \frac{\partial R}{\partial t} - i\tau R e^{-i\psi} \frac{\partial \psi}{\partial t} = \alpha_1 I_3 e^{-i\pi} R^3 e^{i\psi} + \alpha_2 R^3 e^{i\psi} + \beta R^2 e^{-2i\psi} + \gamma I_3 e^{-3i\frac{\pi}{3}} R^2 e^{2i\psi} + \delta R^2 + \epsilon R e^{-i\psi},$$

which is equivalent to

$$\tau \frac{\partial R}{\partial t} - i\tau R \frac{\partial \psi}{\partial t} = \alpha_1 I_3 e^{-i\pi} R^3 e^{2i\psi} + \alpha_2 R^3 e^{2i\psi} + \beta R^2 e^{-i\psi} + \gamma I_3 e^{-3i\frac{\pi}{3}} R^2 e^{3i\psi} + \delta R^2 e^{i\psi} + \epsilon R,$$

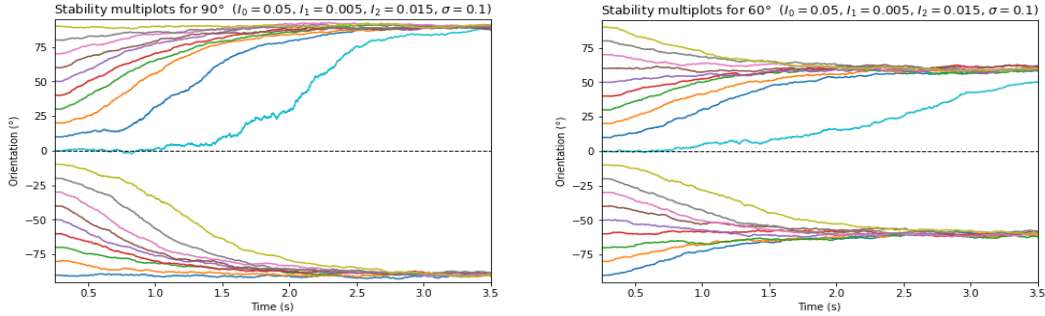
Splitting the equation in its real and imaginary parts leads again to a system of two coupled ordinary differential equations, which are

$$\begin{aligned} \tau \frac{\partial R}{\partial t} & \approx \gamma I_3 R^2 \cos \left(3 \left(\psi - \frac{\pi}{3} \right) \right) + \delta R^2 \cos \psi + \epsilon R, \\ \tau \frac{\partial \psi}{\partial t} & \approx -\gamma I_3 R \sin \left(3 \left(\psi - \frac{\pi}{3} \right) \right) - \delta R \sin \psi, \end{aligned}$$

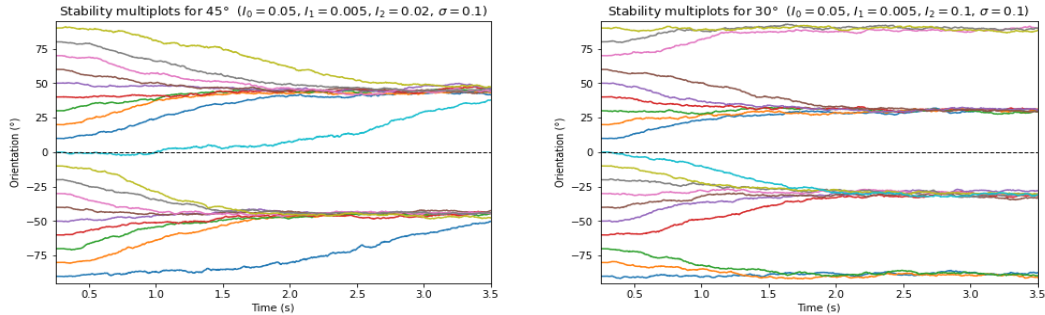
Stability plots

Once we have derived the dynamical system of the amplitude and phase of the bump for the four first Fourier mode inputs, it is also interesting analysing the stable fix points of the differential equation concerning the phase of the bump, because we remind that,

as the authors showed in [3], a continuous attractor network can integrate a circular stimulus feature and track the stimulus average in the phase of its activity bump. Therefore, as one of our main goals was to understand how the network could integrate different higher Fourier order inputs or decision signals, one of the most efficient ways is looking at the temporal evolution of the phase of the bump while the ring network is integrating the different decision signals. With this goal, we set 19 different initial conditions for the phase of the bump, from 90 to -90 degrees with a gap of 10 degrees between the different initial conditions. Thus, in Figure 2.2a we can see that the phase of the bump evolves towards $\pm\frac{\pi}{2}$, depending on if initially the phase was positive or negative, and in the case of initial condition with null phase, the noise is determinant in the evolution. Something very similar happens with Figures 2.2b, 2.2c, where we can see that the phase of the bump evolves towards $\pm\frac{\pi}{3}$ and $\pm\frac{\pi}{4}$, respectively, that is the expected normal behaviour. Finally, in Figure 2.2d, which is a case we have not studied analytically but which we will see in the following chapter is the one that fits more accurately the psychophysical data, we can see that the phase of the bump evolves towards $\pm\frac{\pi}{6}$ if the initial conditions are below $\frac{\pi}{3}$, but if the phase of the bump is initially greater, in absolute value, than this value then the stable point becomes $\pm\frac{\pi}{2}$. As a conclusion, we can see that effectively the phase of the bump evolves towards the expected stable fix points of the different Fourier order spatially modulated inputs.



(a) Stability plot for different initial conditions for a decision signal of second Fourier order (b) Stability plot for different initial conditions for a decision signal of third Fourier order.



(c) Stability plot for different initial conditions for a decision signal of fourth Fourier order. (d) Stability plot for different initial conditions for a decision signal of sixth Fourier order.

Modeling the Jazayeri-Movshon experiment

In this last section we will study, using the bump attractor model introduced, the neural mechanisms underlying the appearance of post decision biases in humans after performing a fine discrimination perceptual task. The main experiment in which we will focus was carried out in the year 2007 by the scientists Mehrdad Jazayeri and J. Anthony Movshon in [7], whose results we will try to explain with the ring network model, where they also proposed a encoding-decoding model so as to explain these phenomena based on their previous work in [8].

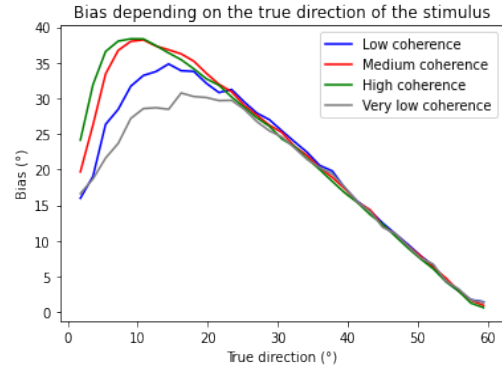
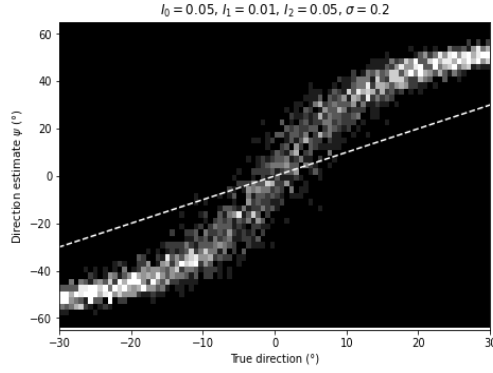
Perceptual illusions are thought to appear depending on the way sensory signals are encoded in the brain, and indeed they are usually used to deduce the mechanisms of sensory encoding information. Nevertheless, this kind of illusions might also arise depending on the way the brain decodes the sensory information processed. Hence, it is known that in fine discrimination tasks, a type of duty where a subject is required to distinguish between two categorical options, such as clockwise or counterclockwise in the case of the random movement of a field of dots, the most reliable information comes from the neurons tuned away from the discrimination boundary, and observers have always been thought to use signals from these displaced neurons from the reference boundary to optimize their performance in the task.

In [7], the authors studied whether using signals from these neurons could also cause a bias in the perception. With this purpose, they carried out an experiment with two stages. The first one consisted on a *fine discrimination* task, where subjects viewed a field of moving dots within a circular aperture and reported whether the direction of motion was clockwise (CW) or counterclockwise (CCW) from a reference boundary indicated by a bar outside the edge of the dotfield, and in second place a *continuous report* task, when subjects were asked to accurately report the direction of motion, their estimates were biased in register with their discrimination choice. Hence, in a

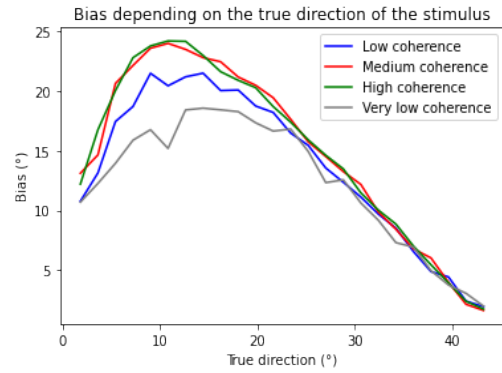
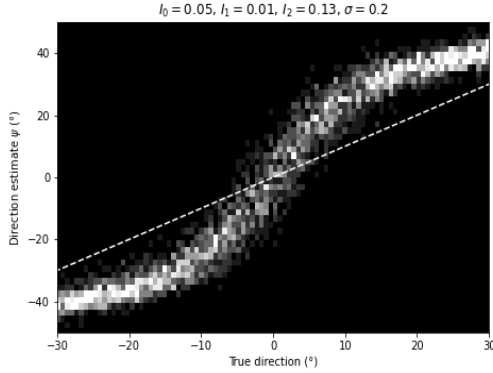
fine direction discrimination task using moving random-dot stimuli, the authors in [7] found that the perception from the observers of the direction of motion was biased away from the boundary. So as to accurately explain this misperception, the authors proposed an encoding-decoding model composed of an encoding and a decoding stage. At the encoding stage, it assumes the sensory representation has a Gaussian probability density function centred at the true direction of motion. The decoding stage computes sensory likelihoods by multiplying the sensory representation with a weighting profile modelled as a gamma density function. The direction estimates are modelled as the peak of the sensory likelihood. The psychophysical results from this experiment can be found in the Appendix B.

Although explained using neural encoding-decoding models and Bayesian principles, it remains unknown what kind of neural network mechanisms give rise to these post-decision biases. With this purpose, in this last section we present the results we obtain after carrying out different simulations so as to check whether a bump attractor network could explain the results from [7]. Further simulation plots can be found in the Appendix C. The simulations consisted on a lapse of time of 500 ms in which the ring network integrated the direction of a random stimulus in a range of $[-30, 30]$ degrees so that a bump could form at this position, and after this integration regime, we presented to the network what is usually call a decision signal of the form $2\bar{I}_4 \cos(4(\theta - \frac{\pi}{4}))$, so as to force the displacement of the bump towards $\pm\frac{\pi}{4}$ radians. As we can appreciate from the three different density plots in Figures 3.1a, 3.1c, 3.1e after these two different integration periods, we can appreciate the same repulsive effect of the estimation away from the reference of zero degrees, which is larger the closer the true direction of the stimulus is to the reference. However, there are slightly differences if we compare them to the plots from Figure B.4, in the case of the psychophysical data one can appreciate much more noise the closer we get to the reference line, and the estimations between clockwise and counterclockwise seems to be disconnected, while in our case there is a transition between these two categorical decisions. If we now look at the bias curves from Figures 3.1b, 3.1d, 3.1f, one can appreciate that the bias increases slightly as we move away from the reference line, and that is slightly larger for higher coherences, contrary to the psychophysical results from [7], until it reaches a peak and then it decreases to zero as we approach to $60^\circ, 45^\circ, 30^\circ$ which are the stable fix points of the second stimulus we have introduced.

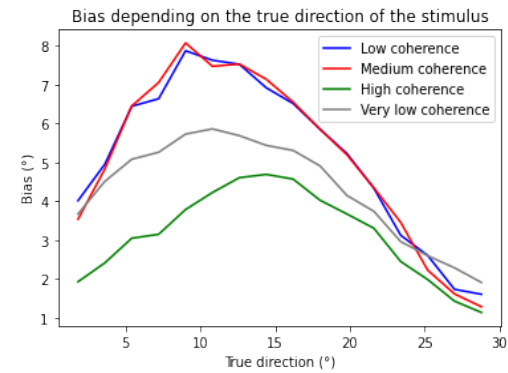
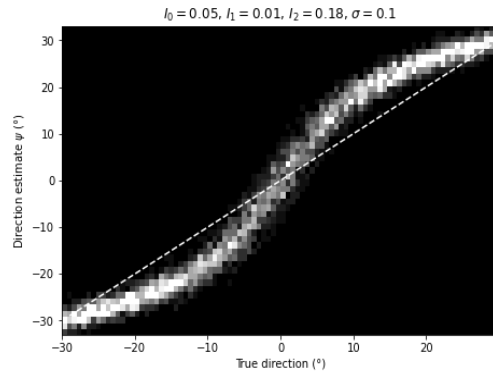
To summarize, we have seen that the ring network model is able to integrate optimally different oriented stimuli and that after integrating higher order Fourier inputs we can force the network to make a categorical decision, which will be more accurate when compared to the psychophysical data the higher the order is.



(a) Density plot of direction estimate versus true direction after the integration of a decision signal of third mode. (b) Bias (difference between estimations and true direction) versus true direction after the integration of a decision signal of third mode.



(c) Density plot of direction estimate versus true direction after the integration of a decision signal of fourth mode. (d) Bias (difference between estimations and true direction) versus true direction after the integration of a decision signal of fourth mode.



(e) Density plot of direction estimate versus true direction after the integration of a decision signal of sixth mode. (f) Bias (difference between estimations and true direction) versus true direction after the integration of a decision signal of sixth mode.

CHAPTER 4

Conclusions

Throughout this thesis we have reviewed one of the canonical continuous attractor models in neuroscience and its underlying bump attractor dynamics. From [3] we already knew that a single population ring network model with a Mexican hat connectivity between its neurons, what gives rise to a bump of activity in the network as explained, could optimally integrate a circular stimulus feature, consisting on a first Fourier order spatially modulated input, and track the stimulus average of the stimulus in the phase of its activity bump. Thus, the first goal of this thesis has been to study how this network could integrate higher order Fourier modulated inputs, from order zero to three. With this purpose, we first had to replicate the calculations carried out in [3] using a multiple scale analysis and a perturbation method. Hence, we obtained the equation of the amplitude equation, a complex-valued magnitude that can be splitted into a real amplitude and a phase, being the latter the magnitude that we have mentioned integrated optimally different orientation stimuli. The results obtained are satisfactory until third order, as the terms that we had to group so as to obtain the dynamics of the amplitude were few, but when it comes to the fourth order we could only make an approximation. Furthermore, although we already know from [3] that the amplitude equation is a very good approximation of the firing rate, further work should be done in this direction with the equation obtained for the second, third and fourth order so as to check numerically the validity of our calculations.

Finally, we applied our theory and used the model to study the possible neural mechanisms underlying the Jazayeri and Movshon experiment, that one can see in Figures B.2, B.3 changing different parameters in the network to replicate different coherence and instead of four six different subjects simulating just one. Hence, as we have discussed the results we quite satisfactory, as we could appreciate the same repulsive effect away from the boundary, although the density plots show slight differences. Further-

more, we have also seen that increasing the order of the Fourier modulated inputs we could obtain more accurate bias curves to those of the psychophysical data, although again not strictly the same because of these differences in the behaviour of the simulation and the data close to the reference line. However, our results were again really satisfying.

APPENDIX A

Mathematical appendix

A.1 Taylor series of the transfer function

In the following section we develop the calculations for the Taylor series expansion of the transfer function, for the three different cases that we consider: homogeneous input, spatially inhomogeneous input and the decision signal. Because the expansion of the perturbation is different for each case, we will develop the calculations explicitly for each one of the signals.

A.1.1 Homogeneous input

$$\begin{aligned}\Phi(x) &= \Phi \left(\sum_{n=0}^{\infty} \langle \omega, r_n \rangle_{\theta} + I_{\text{cr}} + \varepsilon^2 I_0 \right) \\ &= \Phi \left(\langle \omega, r_0 \rangle_{\theta} + \varepsilon \langle \omega, r_1 \rangle_{\theta} + \varepsilon^2 \langle \omega, r_2 \rangle_{\theta} + \mathcal{O}(\varepsilon^3) + I_{\text{cr}} + \varepsilon^2 I_0 \right) . \\ &= \Phi \left(\langle \omega, r_0 \rangle_{\theta} + I_{\text{cr}} + \varepsilon \left(\langle \omega, r_1 \rangle_{\theta} + \varepsilon \left(\langle \omega, r_2 \rangle_{\theta} + I_0 \right) + \varepsilon^2 \langle \omega, r_3 \rangle_{\theta} + \mathcal{O}(\varepsilon^3) \right) \right) .\end{aligned}$$

If we note that $x_0 = \omega_0 r_0 + I_{\text{cr}} = \langle \omega, r_0 \rangle_{\theta} + I_{\text{cr}}$, then

$$\begin{aligned}\Phi(x) &= \Phi_0 + \Phi_0^{(1)} \left(\varepsilon \langle \omega, r_1 \rangle_{\theta} + \varepsilon^2 \left(\langle \omega, r_2 \rangle_{\theta} + I_0 \right) + \varepsilon^3 \langle \omega, r_3 \rangle_{\theta} + \mathcal{O}(\varepsilon^4) \right) \\ &\quad + \frac{1}{2} \Phi_0^{(2)} \left(\varepsilon \langle \omega, r_1 \rangle_{\theta} + \varepsilon^2 \left(\langle \omega, r_2 \rangle_{\theta} + I_0 \right) + \mathcal{O}(\varepsilon^3) \right)^2 \\ &\quad + \frac{1}{6} \Phi_0^{(3)} \left(\varepsilon \langle \omega, r_1 \rangle_{\theta} + \mathcal{O}(\varepsilon^2) \right)^3 + \mathcal{O}(\varepsilon^4),\end{aligned}$$

and by regrouping around the successive powers of ε we get that

$$\begin{aligned}
\Phi(x) &= \Phi_0 + \varepsilon \Phi_0^{(1)} \langle \omega, r_1 \rangle_\theta \\
&\quad + \varepsilon^2 \left(\Phi_0^{(1)} (\langle \omega, r_2 \rangle_\theta + I_0) + \frac{\Phi_0^{(2)}}{2} \langle \omega, r_1 \rangle_\theta^2 \right) \\
&\quad + \varepsilon^3 \left(\Phi_0^{(1)} \langle \omega, r_3 \rangle_\theta + \Phi_0^{(2)} \langle \omega, r_1 \rangle_\theta (\langle \omega, r_2 \rangle_\theta + I_0) + \frac{\Phi_0^{(3)}}{6} \langle \omega, r_1 \rangle_\theta^3 \right) + \mathcal{O}(\varepsilon^4).
\end{aligned} \tag{A.1}$$

A.1.2 First order Fourier spatially inhomogeneous perturbation

Consider now that we expand the ring equation over the input $I(\theta) = I_{\text{cr}} + \varepsilon^2 I_0 + 2\varepsilon^3 \bar{I}_1 \cos(\theta - \theta^*)$. Therefore, the Taylor series expansion of the transfer function becomes

$$\begin{aligned}
\Phi(x) &= \Phi \left(\sum_{n=0}^{\infty} \langle \omega, r_n \rangle_\theta + I_{\text{cr}} + \varepsilon^2 I_0 + 2\varepsilon^3 \bar{I}_1 \cos(\theta - \theta^*) \right) \\
&= \Phi \left(\langle \omega, r_0 \rangle_\theta + \varepsilon \langle \omega, r_1 \rangle_\theta + \varepsilon^2 \langle \omega, r_2 \rangle_\theta + \mathcal{O}(\varepsilon^3) + I_{\text{cr}} + \varepsilon^2 I_0 + 2\varepsilon^3 \bar{I}_1 \cos(\theta - \theta^*) \right) \\
&= \Phi \left(\langle \omega, r_0 \rangle_\theta + I_{\text{cr}} + \varepsilon \left(\langle \omega, r_1 \rangle_\theta + \varepsilon (\langle \omega, r_2 \rangle_\theta + I_0) + \varepsilon^2 (\langle \omega, r_3 \rangle_\theta + 2\bar{I}_1 \cos(\theta - \theta^*)) + \mathcal{O}(\varepsilon^3) \right) \right).
\end{aligned}$$

Again, if we note that $x_0 = \omega_0 r_0 + I_{\text{cr}} = \langle \omega, r_0 \rangle_\theta + I_{\text{cr}}$, then

$$\begin{aligned}
\Phi(x) &= \Phi_0 + \Phi_0^{(1)} (\varepsilon \langle \omega, r_1 \rangle_\theta + \varepsilon^2 (\langle \omega, r_2 \rangle_\theta + I_0) + \varepsilon^3 (\langle \omega, r_3 \rangle_\theta + 2\bar{I}_1 \cos(\theta - \theta^*)) + \mathcal{O}(\varepsilon^4)) \\
&\quad + \frac{1}{2} \Phi_0^{(2)} (\varepsilon \langle \omega, r_1 \rangle_\theta + \varepsilon^2 (\langle \omega, r_2 \rangle_\theta + I_0) + \mathcal{O}(\varepsilon^3))^2 \\
&\quad + \frac{1}{6} \Phi_0^{(3)} (\varepsilon \langle \omega, r_1 \rangle_\theta + \mathcal{O}(\varepsilon^2))^3 + \mathcal{O}(\varepsilon^4),
\end{aligned}$$

and by regrouping around the successive powers of ε we get that

$$\begin{aligned}
\Phi(x) &= \Phi_0 + \varepsilon \Phi_0^{(1)} \langle \omega, r_1 \rangle_\theta \\
&\quad + \varepsilon^2 \left(\Phi_0^{(1)} (\langle \omega, r_2 \rangle_\theta + I_0) + \frac{\Phi_0^{(2)}}{2} \langle \omega, r_1 \rangle_\theta^2 \right) \\
&\quad + \varepsilon^3 \left(\Phi_0^{(1)} (\langle \omega, r_3 \rangle_\theta + 2\bar{I}_1 \cos(\theta - \theta^*)) + \Phi_0^{(2)} \langle \omega, r_1 \rangle_\theta (\langle \omega, r_2 \rangle_\theta + I_0) + \frac{\Phi_0^{(3)}}{6} \langle \omega, r_1 \rangle_\theta^3 \right) \\
&\quad + \mathcal{O}(\varepsilon^4).
\end{aligned} \tag{A.2}$$

A.1.3 Second order Fourier spatially inhomogeneous perturbation

Consider now that we expand the ring equation over the input $I(\theta) = I_{\text{cr}} + \varepsilon^2 I_0 + 2\varepsilon^2 \bar{I}_2 \cos\left(2\left(\theta - \frac{\pi}{2}\right)\right)$. As we mentioned before, the change of the order of expansion of the modulated input is due to the fact that performing the expansion over order 3 decouples the temporal dynamics of the amplitude of the bump from the input, while this does not happen with order 2. Therefore, the Taylor series expansion of the transfer function becomes

$$\begin{aligned}\Phi(x) &= \Phi\left(\sum_{n=0}^{\infty} \langle \omega, r_n \rangle_{\theta} + I_{\text{cr}} + \varepsilon^2 \left(I_0 + 2\bar{I}_2 \cos\left(2\left(\theta - \frac{\pi}{2}\right)\right)\right)\right) \\ &= \Phi\left(\langle \omega, r_0 \rangle_{\theta} + \varepsilon \langle \omega, r_1 \rangle_{\theta} + \varepsilon^2 \langle \omega, r_2 \rangle_{\theta} + \mathcal{O}(\varepsilon^3) + I_{\text{cr}} + \varepsilon^2 \left(I_0 + 2\bar{I}_2 \cos\left(2\left(\theta - \frac{\pi}{2}\right)\right)\right)\right) \\ &= \Phi\left(\langle \omega, r_0 \rangle_{\theta} + I_{\text{cr}} + \varepsilon \left(\langle \omega, r_1 \rangle_{\theta} + \varepsilon \left(\langle \omega, r_2 \rangle_{\theta} + I_0 + 2\bar{I}_2 \cos\left(2\left(\theta - \frac{\pi}{2}\right)\right)\right) + \varepsilon^2 \langle \omega, r_3 \rangle_{\theta} + \mathcal{O}(\varepsilon^3)\right)\right).\end{aligned}$$

Again, if we note that $x_0 = \omega_0 r_0 + I_{\text{cr}} = \langle \omega, r_0 \rangle_{\theta} + I_{\text{cr}}$, then

$$\begin{aligned}\Phi(x) &= \Phi_0 + \Phi_0^{(1)} \left(\varepsilon \langle \omega, r_1 \rangle_{\theta} + \varepsilon^2 \left(\langle \omega, r_2 \rangle_{\theta} + I_0 + 2\bar{I}_2 \cos\left(2\left(\theta - \frac{\pi}{2}\right)\right) \right) + \varepsilon^3 \langle \omega, r_3 \rangle_{\theta} + \mathcal{O}(\varepsilon^4) \right) \\ &\quad + \frac{1}{2} \Phi_0^{(2)} \left(\varepsilon \langle \omega, r_1 \rangle_{\theta} + \varepsilon^2 \left(\langle \omega, r_2 \rangle_{\theta} + I_0 + 2\bar{I}_2 \cos\left(2\left(\theta - \frac{\pi}{2}\right)\right) \right) + \mathcal{O}(\varepsilon^3) \right)^2 \\ &\quad + \frac{1}{6} \Phi_0^{(3)} \left(\varepsilon \langle \omega, r_1 \rangle_{\theta} + \mathcal{O}(\varepsilon^2) \right)^3 + \mathcal{O}(\varepsilon^4),\end{aligned}$$

and by regrouping around the successive powers of ε we get that

$$\begin{aligned}\Phi(x) &= \Phi_0 + \varepsilon \Phi_0^{(1)} \langle \omega, r_1 \rangle_{\theta} \\ &\quad + \varepsilon^2 \left(\Phi_0^{(1)} \left(\langle \omega, r_2 \rangle_{\theta} + I_0 + 2\bar{I}_2 \cos\left(2\left(\theta - \frac{\pi}{2}\right)\right) \right) + \frac{\Phi_0^{(2)}}{2} \langle \omega, r_1 \rangle_{\theta}^2 \right) \\ &\quad + \varepsilon^3 \left(\Phi_0^{(1)} \langle \omega, r_3 \rangle_{\theta} + \Phi_0^{(2)} \langle \omega, r_1 \rangle_{\theta} (\langle \omega, r_2 \rangle_{\theta} + I_0) + \frac{\Phi_0^{(3)}}{6} \langle \omega, r_1 \rangle_{\theta}^3 \right) \\ &\quad + \mathcal{O}(\varepsilon^4).\end{aligned}\tag{A.3}$$

A.1.4 Third order Fourier spatially inhomogeneous perturbation

Consider now that we expand the ring equation over the input $I(\theta) = I_{\text{cr}} + \varepsilon^2 I_0 + \varepsilon 2\bar{I}_3 \cos\left(3\left(\theta - \frac{\pi}{3}\right)\right)$. Again, the change in the order of the perturbation of the modulated input is due the fact that order three decouples the effect of the perturbation onto the dynamics of the amplitude of the bump. Then, the Taylor series expansion of the

transfer function at the critical fix point is

$$\begin{aligned}
\Phi(x) &= \Phi \left(\sum_{n=0}^{\infty} \varepsilon^n \langle \omega, r_n \rangle_{\theta} + I_{\text{cr}} + \varepsilon^2 I_0 + \varepsilon^2 \bar{I}_3 \cos \left(3 \left(\theta - \frac{\pi}{3} \right) \right) \right) \\
&= \Phi \left(\langle \omega, r_0 \rangle_{\theta} + \varepsilon \langle \omega, r_1 \rangle_{\theta} + \varepsilon^2 \langle \omega, r_2 \rangle_{\theta} + \mathcal{O}(\varepsilon^3) + I_{\text{cr}} + \varepsilon \bar{I}_3 \cos \left(3 \left(\theta - \frac{\pi}{3} \right) \right) + \varepsilon^2 I_0 \right) \\
&= \Phi \left(\langle \omega, r_0 \rangle_{\theta} + I_{\text{cr}} + \varepsilon \left(\langle \omega, r_1 \rangle_{\theta} + 2 \bar{I}_3 \cos \left(3 \left(\theta - \frac{\pi}{3} \right) \right) + \varepsilon (\langle \omega, r_2 \rangle_{\theta} + I_0) + \varepsilon^2 \langle \omega, r_3 \rangle_{\theta} + \mathcal{O}(\varepsilon^3) \right) \right)
\end{aligned}$$

Again, if we note that $x_0 = \omega_0 r_0 + I_{\text{cr}} = \langle \omega, r_0 \rangle_{\theta} + I_{\text{cr}}$, then

$$\begin{aligned}
\Phi(x) &= \Phi_0 + \Phi_0^{(1)} \left(\varepsilon \left(\langle \omega, r_1 \rangle_{\theta} + 2 \bar{I}_3 \cos \left(3 \left(\theta - \frac{\pi}{3} \right) \right) \right) + \varepsilon^2 (\langle \omega, r_2 \rangle_{\theta} + I_0) + \varepsilon^3 \langle \omega, r_3 \rangle_{\theta} + \mathcal{O}(\varepsilon^4) \right) \\
&\quad + \frac{1}{2} \Phi_0^{(2)} \left(\varepsilon \left(\langle \omega, r_1 \rangle_{\theta} + 2 \bar{I}_3 \cos \left(3 \left(\theta - \frac{\pi}{3} \right) \right) \right) + \varepsilon^2 (\langle \omega, r_2 \rangle_{\theta} + I_0) + \mathcal{O}(\varepsilon^3) \right)^2 \\
&\quad + \frac{1}{6} \Phi_0^{(3)} \left(\varepsilon \left(\langle \omega, r_1 \rangle_{\theta} + 2 \bar{I}_3 \cos \left(3 \left(\theta - \frac{\pi}{3} \right) \right) \right) + \mathcal{O}(\varepsilon^2) \right)^3 + \mathcal{O}(\varepsilon^4),
\end{aligned}$$

and by regrouping around the successive powers of ε we get that

$$\begin{aligned}
\Phi(x) &= \Phi_0 + \varepsilon \Phi_0^{(1)} \left(\langle \omega, r_1 \rangle_{\theta} + 2 \bar{I}_3 \cos \left(3 \left(\theta - \frac{\pi}{3} \right) \right) \right) \\
&\quad + \varepsilon^2 \left(\Phi_0^{(1)} (\langle \omega, r_2 \rangle_{\theta} + I_0) + \frac{\Phi_0^{(2)}}{2} \left(\langle \omega, r_1 \rangle_{\theta} + 2 \bar{I}_3 \cos \left(3 \left(\theta - \frac{\pi}{3} \right) \right) \right)^2 \right) \\
&\quad + \varepsilon^3 \left(\Phi_0^{(1)} \langle \omega, r_3 \rangle_{\theta} + \Phi_0^{(2)} \left(\langle \omega, r_1 \rangle_{\theta} + 2 \bar{I}_3 \cos \left(3 \left(\theta - \frac{\pi}{3} \right) \right) \right) (\langle \omega, r_2 \rangle_{\theta} + I_0) \right) \\
&\quad + \varepsilon^3 \left(\frac{\Phi_0^{(3)}}{6} \left(\langle \omega, r_1 \rangle_{\theta} + 2 \bar{I}_3 \cos \left(3 \left(\theta - \frac{\pi}{3} \right) \right) \right)^3 \right) \\
&\quad + \mathcal{O}(\varepsilon^4).
\end{aligned} \tag{A.4}$$

In this case, it will be useful to compute $\left(\langle \omega, r_1 \rangle_{\theta} + \left(I_3 e^{3i(\theta - \frac{\pi}{3})} + I_3^* e^{-3i(\theta - \frac{\pi}{3})} \right) \right)^2$, where $\langle \omega, r_1 \rangle_{\theta} = \omega_1 r_{11} e^{i\theta} + \omega_1^* r_{11}^* e^{-i\theta} + \omega_3 r_{13} e^{3i\theta} + \omega_3^* r_{13}^* e^{-3i\theta}$, $r_{11} = A$, $r_{13} = \frac{AI_3}{1 - \omega_3 \Phi_0^{(1)}}$. Now,

$$\begin{aligned}
&\left(\langle \omega, r_1 \rangle_{\theta} + \left(I_3 e^{3i(\theta - \frac{\pi}{3})} + I_3^* e^{-3i(\theta - \frac{\pi}{3})} \right) \right)^2 = \\
&\langle \omega, r_1 \rangle_{\theta}^2 + 2 \langle \omega, r_1 \rangle_{\theta} \left(I_3 e^{3i(\theta - \frac{\pi}{3})} + I_3^* e^{-3i(\theta - \frac{\pi}{3})} \right) + \left(I_3 e^{3i(\theta - \frac{\pi}{3})} + I_3^* e^{-3i(\theta - \frac{\pi}{3})} \right)^2 =,
\end{aligned}$$

where

$$\begin{aligned}
\langle \omega, r_1 \rangle_\theta^2 &= \omega_1^2 r_{11}^2 e^{2i\theta} + (\omega_1^*)^2 (r_{11}^*)^2 e^{-2i\theta} + \omega_3^2 r_{13}^2 e^{6i\theta} + (\omega_3^*)^2 (r_{13}^*)^2 e^{-6i\theta} + \\
&\quad |\omega_1|^2 |r_{11}|^2 + \omega_1 r_{11} \omega_3 r_{13} e^{4i\theta} + \omega_1 r_{11} \omega_3^* r_{13}^* e^{-2i\theta} + \\
&\quad \omega_1^* r_{11}^* \omega_3 r_{13} e^{2i\theta} + \omega_1^* r_{11}^* \omega_3^* r_{13}^* e^{-4i\theta} + |\omega_3|^2 |r_{13}|^2 \\
&= |\omega_1|^2 |r_{11}|^2 + \left(\omega_1^2 r_{11}^2 e^{2i\theta} + (\omega_1^*)^2 (r_{11}^*)^2 e^{-2i\theta} \right) + \\
&\quad \left(\omega_1 r_{11} \omega_3 r_{13} e^{4i\theta} + \omega_1^* r_{11}^* \omega_3^* r_{13}^* e^{-4i\theta} \right) + \left(\omega_1^* r_{11}^* \omega_3 r_{13} e^{2i\theta} + \omega_1 r_{11} \omega_3^* r_{13}^* e^{-2i\theta} \right) + \\
&\quad \left(\omega_3^2 r_{13}^2 e^{6i\theta} + (\omega_3^*)^2 (r_{13}^*)^2 e^{-6i\theta} \right) + |\omega_3|^2 |r_{13}|^2,
\end{aligned}$$

so we note that this term contains terms of order zero, two, four and six. Regarding $2\langle \omega, r_1 \rangle_\theta \left(I_3 e^{3i(\theta - \frac{\pi}{3})} + I_3^* e^{-3i(\theta - \frac{\pi}{3})} \right)$, we note that

$$\begin{aligned}
\langle \omega, r_1 \rangle_\theta \left(I_3 e^{3i(\theta - \frac{\pi}{3})} + I_3^* e^{-3i(\theta - \frac{\pi}{3})} \right) &= \omega_1 r_{11} I_3 e^{-3i\frac{\pi}{3}} e^{4i\theta} + \omega_1^* r_{11}^* I_3^* e^{3i\frac{\pi}{3}} e^{-4i\theta} + \\
&\quad \omega_1^* r_{11}^* I_3 e^{-3i\frac{\pi}{3}} e^{2i\theta} + \omega_1 r_{11} I_3^* e^{3i\frac{\pi}{3}} e^{-2i\theta} + \\
&\quad \omega_3 r_{13} I_3 e^{-3i\frac{\pi}{3}} e^{6i\theta} + \omega_3^* r_{13}^* I_3^* e^{3i\frac{\pi}{3}} e^{-6i\theta} + \\
&\quad \omega_3^* r_{13}^* I_3 e^{-3i\frac{\pi}{3}} + \omega_3 r_{13} I_3^* e^{3i\frac{\pi}{3}},
\end{aligned}$$

and finally

$$\left(I_3 e^{3i(\theta - \frac{\pi}{3})} + I_3^* e^{-3i(\theta - \frac{\pi}{3})} \right)^2 = I_3^2 e^{-6i\frac{\pi}{3}} e^{6i\theta} + (I_3^*)^2 e^{6i\frac{\pi}{3}} e^{-6i\theta} + |I_3|^2,$$

and hence the quadratic expression is a combination of terms of zeroth, second, fourth and sixth order.

A.1.5 Fourth order Fourier spatially inhomogeneous perturbation

Consider now that we expand the ring equation over the input $I(\theta) = I_{\text{cr}} + \varepsilon I_0 + \varepsilon 2\bar{I}_4 \cos(4(\theta - \frac{\pi}{4}))$. Again, the change in the order of the perturbation of the modulated input is due the fact that order three decouples the effect of the perturbation onto the dynamics of the amplitude of the bump. Then, the Taylor series expansion of the transfer function at the critical fix point is

$$\begin{aligned}
\Phi(x) &= \Phi \left(\sum_{n=0}^{\infty} \varepsilon^n \langle \omega, r_n \rangle_\theta + I_{\text{cr}} + \varepsilon I_0 + \varepsilon 2\bar{I}_4 \cos \left(4 \left(\theta - \frac{\pi}{4} \right) \right) \right) \\
&= \Phi \left(\langle \omega, r_0 \rangle_\theta + \varepsilon \langle \omega, r_1 \rangle_\theta + \varepsilon^2 \langle \omega, r_2 \rangle_\theta + \mathcal{O}(\varepsilon^3) + I_{\text{cr}} + \varepsilon 2\bar{I}_4 \cos \left(4 \left(\theta - \frac{\pi}{4} \right) \right) + \varepsilon I_0 \right) \\
&= \Phi \left(\langle \omega, r_0 \rangle_\theta + I_{\text{cr}} + \varepsilon \left(\langle \omega, r_1 \rangle_\theta + I_0 + 2\bar{I}_4 \cos \left(4 \left(\theta - \frac{\pi}{4} \right) \right) + \varepsilon \langle \omega, r_2 \rangle_\theta + \varepsilon^2 \langle \omega, r_3 \rangle_\theta + \mathcal{O}(\varepsilon^3) \right) \right).
\end{aligned}$$

Again, if we note that $x_0 = \omega_0 r_0 + I_{\text{cr}} = \langle \omega, r_0 \rangle_\theta + I_{\text{cr}}$, then

$$\begin{aligned} \Phi(x) = & \Phi_0 + \Phi_0^{(1)} \left(\varepsilon \left(\langle \omega, r_1 \rangle_\theta + I_0 + 2\bar{I}_4 \cos \left(4 \left(\theta - \frac{\pi}{4} \right) \right) \right) + \varepsilon^2 \langle \omega, r_2 \rangle_\theta + \varepsilon^3 \langle \omega, r_3 \rangle_\theta + \varepsilon^4 \langle \omega, r_4 \rangle_\theta + \mathcal{O}(\varepsilon^5) \right) \\ & + \frac{1}{2} \Phi_0^{(2)} \left(\varepsilon \left(\langle \omega, r_1 \rangle_\theta + I_0 + 2\bar{I}_4 \cos \left(4 \left(\theta - \frac{\pi}{4} \right) \right) \right) + \varepsilon^2 \langle \omega, r_2 \rangle_\theta + \varepsilon^3 \langle \omega, r_3 \rangle_\theta + \mathcal{O}(\varepsilon^4) \right)^2 + \mathcal{O}(x^3), \end{aligned}$$

and by regrouping around the successive powers of ε we get that

$$\begin{aligned} \Phi(x) = & \Phi_0 + \varepsilon \Phi_0^{(1)} \left(\langle \omega, r_1 \rangle_\theta + I_0 + 2\bar{I}_4 \cos \left(4 \left(\theta - \frac{\pi}{4} \right) \right) \right) \\ & + \varepsilon^2 \left(\Phi_0^{(1)} \langle \omega, r_2 \rangle_\theta + \frac{\Phi_0^{(2)}}{2} \left(\langle \omega, r_1 \rangle_\theta + I_0 + 2\bar{I}_4 \cos \left(4 \left(\theta - \frac{\pi}{4} \right) \right) \right)^2 \right) \\ & + \varepsilon^3 \left(\Phi_0^{(1)} \langle \omega, r_3 \rangle_\theta + \Phi_0^{(2)} \left(\langle \omega, r_1 \rangle_\theta + I_0 + 2\bar{I}_4 \cos \left(4 \left(\theta - \frac{\pi}{4} \right) \right) \right) \langle \omega, r_2 \rangle_\theta \right) \\ & + \varepsilon^4 \left(\Phi_0^{(1)} \langle \omega, r_4 \rangle_\theta + \Phi_0^{(2)} \left(\langle \omega, r_1 \rangle_\theta + I_0 + 2\bar{I}_4 \cos \left(4 \left(\theta - \frac{\pi}{4} \right) \right) \right) \langle \omega, r_3 \rangle_\theta + \frac{\Phi_0^{(2)}}{2} \langle \omega, r_2 \rangle_\theta^2 \right), \end{aligned} \quad (\text{A.5})$$

Similarly to what happened with the third Fourier mode, it will be useful to compute $\left(\langle \omega, r_1 \rangle_\theta + I_0 + \left(I_4 e^{4i(\theta - \frac{\pi}{4})} + I_4^* e^{-4i(\theta - \frac{\pi}{4})} \right) \right)^2$, where $\langle \omega, r_1 \rangle_\theta = \omega_0 r_{10} + \omega_1 r_{11} e^{i\theta} + \omega_1^* r_{11}^* e^{-i\theta} + \omega_4 r_{14} e^{4i\theta} + \omega_4^* r_{14}^* e^{-4i\theta}$, $r_{10} = I_0$, $r_{11} = A$, $r_{14} = \frac{AI_4}{1 - \omega_4 \Phi_0^{(1)}}$. Now,

$$\begin{aligned} & \left(\langle \omega, r_1 \rangle_\theta + I_0 + \left(I_4 e^{4i(\theta - \frac{\pi}{4})} + I_4^* e^{-4i(\theta - \frac{\pi}{4})} \right) \right)^2 = \\ & \langle \omega, r_1 \rangle_\theta^2 + 2\langle \omega, r_1 \rangle_\theta \left(I_4 e^{4i(\theta - \frac{\pi}{4})} + I_4^* e^{-4i(\theta - \frac{\pi}{4})} \right) + \left(I_4 e^{4i(\theta - \frac{\pi}{4})} + I_4^* e^{-4i(\theta - \frac{\pi}{4})} \right)^2 + \\ & 2\langle \omega, r_1 \rangle_\theta I_0 + I_0 I_4 e^{4i(\theta - \frac{\pi}{4})} + I_0 I_4^* e^{-4i(\theta - \frac{\pi}{4})} + I_0^2, \end{aligned} \quad (\text{A.6})$$

where

$$\begin{aligned}
\langle \omega, r_1 \rangle_\theta^2 &= \left(\omega_0 r_{10} + \omega_1 r_{11} e^{i\theta} + \omega_1^* r_{11}^* e^{-i\theta} + \omega_4 r_{14} e^{4i\theta} + \omega_4^* r_{14}^* e^{-4i\theta} \right)^2 = \\
&= \omega_0^2 r_{10}^2 + \omega_1^2 r_{11}^2 e^{2i\theta} + (\omega_1^*)^2 (r_{11}^*)^2 e^{-2i\theta} + \omega_4^2 r_{14}^2 e^{8i\theta} + (\omega_4^*)^2 (r_{14}^*)^2 e^{-8i\theta} + \\
&\quad 2\omega_0 r_{10} \omega_1 r_{11} e^{i\theta} + 2\omega_0 r_{10} \omega_1^* r_{11}^* e^{-i\theta} + 2\omega_0 r_{10} \omega_4 r_{14} e^{4i\theta} + 2\omega_0 r_{10} \omega_4^* r_{14}^* e^{-4i\theta} \\
&\quad 2|\omega_1|^2 |r_{11}|^2 + 2\omega_1 r_{11} \omega_4 r_{14} e^{5i\theta} + 2\omega_1 r_{11} \omega_4^* r_{14}^* e^{-3i\theta} + \\
&\quad 2\omega_1^* r_{11}^* \omega_4 r_{14} e^{3i\theta} + 2\omega_1^* r_{11}^* \omega_4^* r_{14}^* e^{-5i\theta} + 2|\omega_4|^2 |r_{14}|^2 = \\
&= \omega_0^2 r_{10}^2 + \left(2\omega_0 r_{10} \omega_1 r_{11} e^{i\theta} + 2\omega_0 r_{10} \omega_1^* r_{11}^* e^{-i\theta} \right) + \left(2\omega_0 r_{10} \omega_4 r_{14} e^{4i\theta} + 2\omega_0 r_{10} \omega_4^* r_{14}^* e^{-4i\theta} \right) + \\
&\quad |\omega_1|^2 |r_{11}|^2 + \left(2\omega_1^2 r_{11}^2 e^{2i\theta} + 2(\omega_1^*)^2 (r_{11}^*)^2 e^{-2i\theta} \right) + \\
&\quad \left(2\omega_1 r_{11} \omega_4 r_{14} e^{5i\theta} + 2\omega_1^* r_{11}^* \omega_4^* r_{14}^* e^{-5i\theta} \right) + \left(2\omega_1^* r_{11}^* \omega_4 r_{14} e^{3i\theta} + 2\omega_1 r_{11} \omega_4^* r_{14}^* e^{-3i\theta} \right) + \\
&\quad \left(2\omega_4^2 r_{14}^2 e^{8i\theta} + 2(\omega_4^*)^2 (r_{14}^*)^2 e^{-8i\theta} \right) + |\omega_4|^2 |r_{14}|^2,
\end{aligned}$$

so we note that this term contains terms of order zero, one, two, three, four, five and eight. Regarding the product $2\langle \omega, r_1 \rangle_\theta \left(I_4 e^{4i(\theta - \frac{\pi}{4})} + I_4^* e^{-4i(\theta - \frac{\pi}{4})} \right)$, we note that

$$\begin{aligned}
\langle \omega, r_1 \rangle_\theta \left(I_4 e^{4i(\theta - \frac{\pi}{4})} + I_4^* e^{-4i(\theta - \frac{\pi}{4})} \right) &= \omega_0 r_{10} I_4 e^{-4i\frac{\pi}{4}} e^{4i\theta} + \omega_0 r_{10} I_4^* e^{4i\frac{\pi}{4}} e^{-4i\theta} + \\
&\quad \omega_1 r_{11} I_4 e^{-4i\frac{\pi}{4}} e^{5i\theta} + \omega_1^* r_{11}^* I_4^* e^{4i\frac{\pi}{4}} e^{-5i\theta} + \\
&\quad \omega_1^* r_{11}^* I_4 e^{-4i\frac{\pi}{4}} e^{3i\theta} + \omega_1 r_{11} I_4^* e^{4i\frac{\pi}{4}} e^{-3i\theta} + \\
&\quad \omega_4 r_{14} I_4 e^{-4i\frac{\pi}{4}} e^{8i\theta} + \omega_4^* r_{14}^* I_4^* e^{4i\frac{\pi}{4}} e^{-8i\theta} + \\
&\quad \omega_4^* r_{14}^* I_4 e^{-4i\frac{\pi}{4}} + \omega_4 r_{14} I_4^* e^{4i\frac{\pi}{4}},
\end{aligned}$$

we can also compute

$$\left(I_4 e^{4i(\theta - \frac{\pi}{4})} + I_4^* e^{-4i(\theta - \frac{\pi}{4})} \right)^2 = I_4^2 e^{-8i\frac{\pi}{4}} e^{8i\theta} + (I_4^*)^2 e^{8i\frac{\pi}{4}} e^{-8i\theta} + |I_4|^2,$$

and finally

$$\langle \omega, r_1 \rangle_\theta I_0 = I_0 \omega_0 r_{10} + I_0 \omega_1 r_{11} e^{i\theta} + I_0 \omega_1^* r_{11}^* e^{-i\theta} + I_0 \omega_4 r_{14} e^{4i\theta} + I_0 \omega_4^* r_{14}^* e^{-4i\theta}$$

and hence the mentioned quadratic expression is a combination of terms of zeroth, first, second, third, fourth, fifth and eighth order.

A.2 Amplitude equation for a Fourth order Fourier input

A.2.1 Derivation of the amplitude equation

Finally, we include in here the calculations for the fourth order Fourier mode input because of space. So as to walk a tight line and try to fit even more accurately the psychophysical data from the experiment carried out in [7], a final option for forcing a decision in the network is to apply a cosinus function of spatial wavenumber $k = 4$, whose fixed points are even closer to the reference, so as we mentioned this will later help us fit more accurately the psychophysical data. In this case, we will expand the ring equation (2.1) over the input

$$I(\theta) = I_{\text{cr}} + \varepsilon I_0 + \varepsilon 2\bar{I}_4 \cos\left(4\left(\theta - \frac{\pi}{4}\right)\right)$$

Again, the change in the order of the perturbation is done only with the purpose of managing to get the effect of the stimulus input in the dynamics of the amplitude of the bump. After calculating the Taylor series expansion of the transfer function in the equation (A.5) in the Appendix A.1, we note that the ring equation (2.1) can be written in a more compact way as

$$(\mathcal{L}_0 + \varepsilon^2 \mathcal{L}_2) \sum_{n=1}^{\infty} \varepsilon^n r_n = \varepsilon 2\bar{I}_4 \cos\left(4\left(\theta - \frac{\pi}{4}\right)\right) + \varepsilon^2 \mathcal{N}_2 + \varepsilon^3 \mathcal{N}_3 + \varepsilon^4 \mathcal{N}_4 + \mathcal{O}(\varepsilon^5), \quad (\text{A.7})$$

where $\mathcal{L}_0, \mathcal{L}_2$ are the same linear operators defined in (2.6) and

$$\mathcal{N}_2 = \Phi_0^{(1)} I_0 + \frac{\Phi_0^{(2)}}{2} \left(\langle \omega, r_1 \rangle_{\theta} + 2\bar{I}_4 \cos\left(4\left(\theta - \frac{\pi}{4}\right)\right) \right)^2,$$

$$\mathcal{N}_3 = \Phi_0^{(2)} \left(\langle \omega, r_1 \rangle_{\theta} + 2\bar{I}_4 \cos\left(4\left(\theta - \frac{\pi}{4}\right)\right) \right) (\langle \omega, r_2 \rangle_{\theta} + I_0)$$

and

$$\mathcal{N}_4 = \Phi_0^{(2)} \left(\langle \omega, r_1 \rangle_{\theta} + 2\bar{I}_4 \cos\left(4\left(\theta - \frac{\pi}{4}\right)\right) \right) \langle \omega, r_3 \rangle_{\theta}$$

The solution of first order r_1 in this case again does change because of the appearance of the terms εI_0 and $\varepsilon 2\bar{I}_4 \cos\left(4\left(\theta - \frac{\pi}{4}\right)\right)$. Now, the linear system to solve is $\mathcal{L}_0 r_1 = \varepsilon(I_0 + 2\bar{I}_4 \cos\left(4\left(\theta - \frac{\pi}{4}\right)\right))$, so it is clear that apart from the first order term that appears in all derivations, $r_{11} = A e^{i\theta}$, there will also be a zeroth and fourth mode in its Fourier series expansion, $r_{10} = I_0 A$, $r_{14} = \frac{A I_4}{1 - \omega_4 \Phi_0^{(1)}} e^{-4i\theta^d}$.

Regarding the second order terms of the equality $\mathcal{O}(\varepsilon^2)$ in (A.7), we have that $\mathcal{L}_0 r_2 = \mathcal{N}_2$, which if we develop becomes

$$r_2 - \Phi_0^{(1)} \langle \omega, r_2 \rangle_{\theta} = \frac{\Phi_0^{(2)}}{2} \left(\langle \omega, r_1 \rangle_{\theta} + I_0 + 2\bar{I}_4 \cos\left(4\left(\theta - \frac{\pi}{4}\right)\right) \right)^2$$

Again, following the development of the quadratic expression in the Appendix A.1, one can appreciate that the right hand side term of the equality is a combination of terms of order zero, one, two, three, four, five and eight, where in particular the term of first order is

$$r_{21} = \frac{\Phi_0^{(2)}}{2} (2\omega_0 r_{10} \omega_1 r_{11} + I_0 \omega_1 r_{11}) = \frac{\Phi_0^{(2)}}{2} (2\omega_0 \omega_1 I_0 + I_0 \omega_1) A,$$

the term of second order is

$$r_{22} = 2\omega_1^2 r_{11}^2 = 2\omega_1^2 A^2$$

and the term of third order is

$$r_{23} = \omega_1^* r_{11}^* \omega_4 r_{14} + \omega_1^* r_{11}^* I_4 e^{-4i\frac{\pi}{4}}.$$

If we now focus in the solution to third order, in other words the terms $\mathcal{O}(\varepsilon^3)$, we have that the linear system to solve is $\mathcal{L}_0 r_3 + \mathcal{L}_2 r_1 = \mathcal{N}_3$, which if we expand becomes

$$r_3 - \Phi_0^{(1)} \langle \omega, r_3 \rangle_\theta + \frac{\partial r_1}{\partial T} = \Phi_0^{(2)} \left(\langle \omega, r_1 \rangle_\theta + I_0 + 2\bar{I}_4 \cos \left(4 \left(\theta - \frac{\pi}{4} \right) \right) \right) \langle \omega, r_2 \rangle_\theta.$$

To ease the reading, as we are replicating the same calculations, we will again only focus looking for the second mode of the third term of the firing rate, instead of the first mode as we have been always doing. In this case, all elements contain terms of second order. Furthermore, the previous equations gets a bit simplified as r_1 does not have second Fourier mode. One can note that combining terms of order five and four, three and two etc we can get many elements of order two for the second Fourier mode of r_3 . However, if we look at $\Phi_0^{(2)} \langle \omega, r_1 \rangle_\theta \langle \omega, r_2 \rangle_\theta$ we see that

$$r_{32}(1 - \omega_2 \Phi_0^{(1)}) = \Phi_0^{(2)} (\omega_0 r_{10} \omega_2 r_{22} + \omega_1 r_{11} \omega_1 r_{21} + \omega_4 r_{14} \omega_2^* r_{22}^* + \omega_1^* r_{11}^* \omega_3^* r_{23}^*) + \Phi_0^{(2)} \left(I_0 \omega_2 r_{22} + I_4 e^{-4i\frac{\pi}{4}} \omega_2^* r_{22}^* \right). \quad (\text{A.8})$$

Finally, we have to go further and analyse the terms of fourth order $\mathcal{O}(\varepsilon^4)$. In this case, the linear system to solve is $\mathcal{L}_0 r_4 + \mathcal{L}_2 r_2 = \mathcal{N}_4$, which if we expand becomes

$$r_4 - \Phi_0^{(1)} \langle \omega, r_4 \rangle_\theta + \frac{\partial r_2}{\partial T} = \Phi_0^{(2)} \left(\langle \omega, r_1 \rangle_\theta + I_0 + 2\bar{I}_4 \cos \left(4 \left(\theta - \frac{\pi}{4} \right) \right) \right) \langle \omega, r_3 \rangle_\theta + \frac{\Phi_0^{(2)}}{2} \langle \omega, r_2 \rangle_\theta^2.$$

Now, we are interested in finding the expression for the first mode of the fourth term of the firing rate, as in the previous equation r_{21} contains the information about the dynamics of the amplitude of the bump. One can note that there are a great variety of combinations that give rise to terms of first order, and so as to ease the reading we will

only focus in a few of them. Thus, in our case we can simplify the expression as

$$\begin{aligned}
\frac{\Phi_0^{(2)}}{2} (2\omega_0\omega_1 I_0 + I_0\omega_1) \frac{\partial A}{\partial T} &\approx \Phi_0^{(2)} \left(\langle \omega, r_1 \rangle_\theta + I_0 + 2\bar{I}_4 \cos \left(4 \left(\theta - \frac{\pi}{4} \right) \right) \right) \langle \omega, r_3 \rangle_\theta \\
&\approx \Phi_0^{(2)} (\omega_1^* r_{11}^* \omega_2 r_{32}) \approx \frac{\left(\Phi_0^{(2)} \right)^2}{1 - \omega_2 \Phi_0^{(1)}} \omega_1^* r_{11}^* I_4 e^{-4i\frac{\pi}{4}} \omega_2^* r_{22}^* \\
&\approx \frac{\left(\Phi_0^{(2)} \right)^2}{1 - \omega_2 \Phi_0^{(1)}} \omega_1^* A^* I_4 e^{-4i\frac{\pi}{4}} \omega_2^* 2(\omega_1^*)^2 (A^*)^2.
\end{aligned} \tag{A.9}$$

Hence, finally the dynamics of the amplitude equation is given by

$$\frac{\partial A}{\partial T} \approx \frac{\Phi_0^{(2)}}{(2\omega_0\omega_1 I_0 + I_0\omega_1) \left(1 - \omega_2 \Phi_0^{(1)} \right)} (\omega_1^*)^3 \omega_2^* I_4 e^{-4i\frac{\pi}{4}} (A^*)^3 \tag{A.10}$$

A.2.2 Dynamics of the amplitude equation

Briefly, we can split the differential equation writing the amplitude in polar notation if we denote it as $A = Re^{-i\psi}$, where R and ψ are respectively the real value amplitude and the phase of the bump. The equation is then

$$\tau e^{-i\psi} \frac{\partial R}{\partial t} - i\tau R e^{-i\psi} \frac{\partial \psi}{\partial t} \approx \alpha I_4 e^{-4i\frac{\pi}{4}} (A^*)^3 = \alpha I_4 e^{-4i\frac{\pi}{4}} R^3 e^{3i\psi}$$

Splitting the equation in its real and imaginary parts leads again to a system of two coupled ODEs,

$$\begin{aligned}
\tau \frac{\partial R}{\partial t} &\approx \alpha I_4 R^3 \cos \left(4 \left(\psi - \frac{\pi}{4} \right) \right), \\
\tau \frac{\partial \psi}{\partial t} &\approx -\alpha I_4 R^2 \sin \left(4 \left(\psi - \frac{\pi}{4} \right) \right).
\end{aligned}$$

One may note that there are a great quantity of terms missing in the developing of this equations, but the main goal of this section has been to understand in a very simplified way the influence of the input in the dynamics of the amplitude and phase of the bump.

APPENDIX B

Jazayeri-Movshon experiment psychophysical results

In this second section from the appendix we present the psychophysical data results from the experiments carried out by Jazayeri and Movshon with the explained two tasks, the fine discrimination and the continuous report, whose scheme can be seen in Figure B.1.

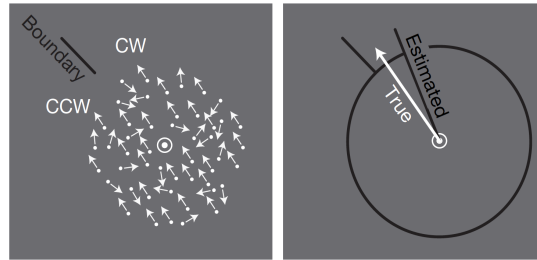


Figure B.1: Left: The discrimination phase. Subjects viewed a field of moving random dots and indicated whether its direction was clockwise (CW) or counter-clockwise (CCW) with respect to an indicated discrimination boundary that varied randomly from trial to trial. Right: The estimation phase. After discriminating the direction of motion, subjects reported their estimate of the direction of motion by extending a dark line from the centre of the display with the computer mouse.

The goal of this section is to allow to compare the results of our simulations with the original data. In Figure B.2 we show the distribution of estimations responses of one of the six different subjects from the experiment, where each column represents the distribution of estimates for a particular true direction of motion. As one can see, when subjects were asked to report the direction of motion, their estimates deviated from the direction of motion in the stimulus, and were biased in register with their dis-

crimination choice. The magnitude of these deviations depended on both the coherence and the direction of motion, being larger for more uncertain conditions when either coherence was low or the direction was close to the boundary, the conditions in which discrimination performance was worst.

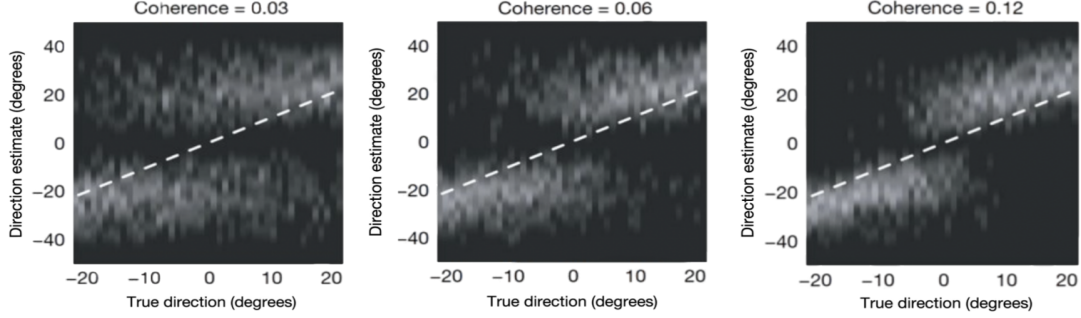


Figure B.2: Figures representing the distribution of estimation responses for one subject at the three coherence levels. Each column of each plot represents the distribution of estimates for a particular true direction of motion.

In second place, another important result are the bias curves, in other words, the difference between the true direction of motion of the coherent dots and the estimated direction of the subject. In the Figure B.3 we show the bias curves for the six different subjects and all three levels of coherence. As one can see from Figure B.2, this bias is larger closer to the reference line and lower as we walk away from this reference.

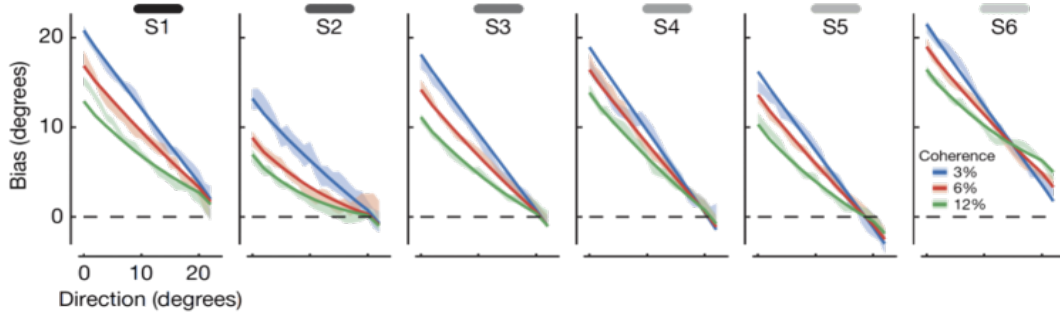


Figure B.3: The mean bias (the difference between the true and estimated directions) \pm one standard error (shading) and the model fits (thick line) for all subjects and all coherence values.

Finally, it is also interesting to show the proportion of categorical reports and the estimate of the direction of motion for a single subject and all three levels of coherence, which we show in Figure B.4.

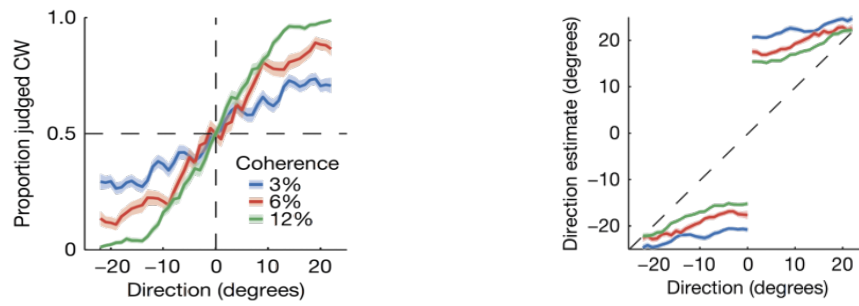


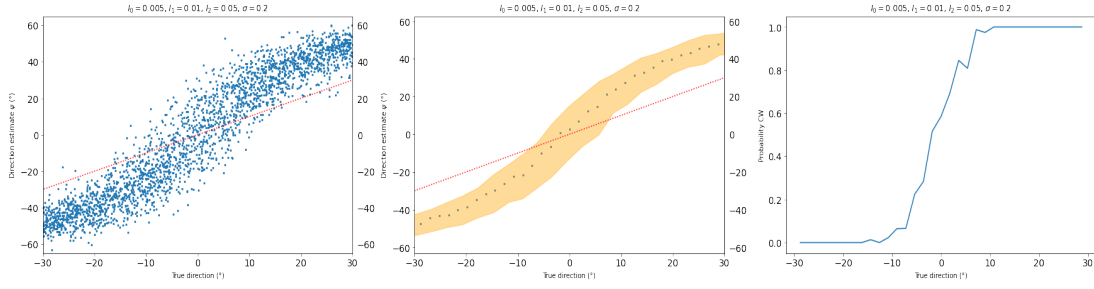
Figure B.4: Left: Proportion of CW judgements (thick lines) and their standard errors (shading) as a function of direction of motion for all coherence values for one subject. Right: Subjective estimates as a function of direction of motion for trials on which motion direction was correctly discriminated.

APPENDIX C

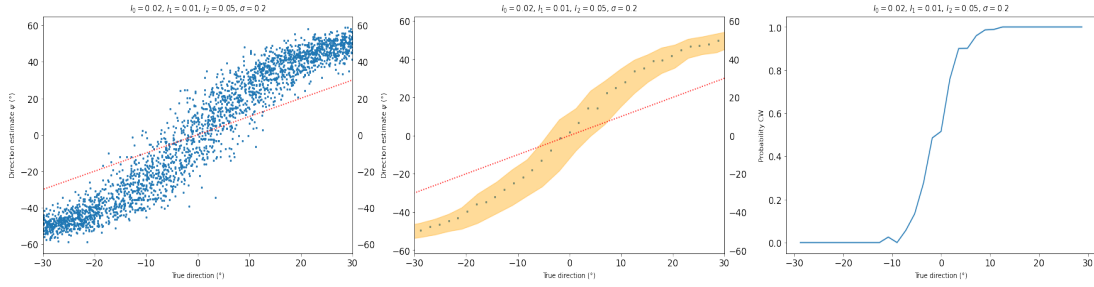
Additional simulation results

In this last section of the appendix we present a large number of graphics that we have carried out and that we have not included in the main section for reasons of space. Essentially, these graphics correspond to simulations of $n = 5000$ trials that consisted on initially presenting a stimulus to the neural network for a period of one second so that it could integrate it and a bump could be formed, and finally presenting a second stimulus for a period of half a second so as to force the movement of the bump, with the aim of making a categorical decision. In Figures C.1, C.2 these trials correspond to a second stimulus of the form $\cos\left(3\left(\theta - \frac{\pi}{3}\right)\right)$. For this particular decision signal, we have ran simulations changing the value of the global excitatory drive $I_0 = 0.005, 0.02, 0.05, 0.08$, that tells us how far we are from the Turing bifurcation. Fitting the Ornstein-Uhlenbeck noise and the different strength of the two stimulus for each trial, we have obtained the plots we show. In Figures C.3, C.4 these trials correspond to a second stimulus of the form $\cos\left(4\left(\theta - \frac{\pi}{4}\right)\right)$ and finally in Figures C.5, C.6 these trials correspond to a second stimulus of the form $\cos\left(6\left(\theta - \frac{\pi}{6}\right)\right)$, where we have again repeated the simulations for the same four different values of I_0 and fitted the strength of the noise and of the stimulus.

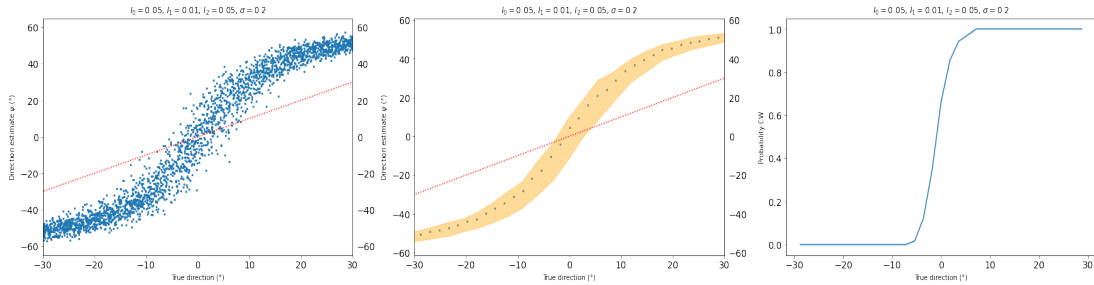
Finally, in Figures C.7, C.8, C.9, C.10 we show a stability plot for the phase of the bump, namely we have ran a one trial simulation in which we presented to the network four different stimulus, so that the bump formed and moved towards them for a period of three seconds and a half, and finally for the same period we presented a decision signal, three of them where the same described above and the first one was a second Fourier mode signal. Hence, with these plots we are able to understand how the phase evolves towards the fix points of the different decision signals presented.



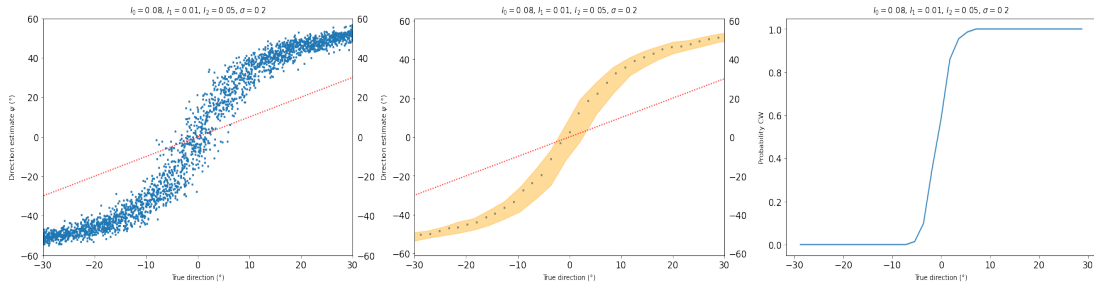
(a) Scatter plot and psychometric curve for very low coherence and a sixth Fourier order input.



(b) Scatter plot and psychometric curve for low coherence and a sixth Fourier order input.

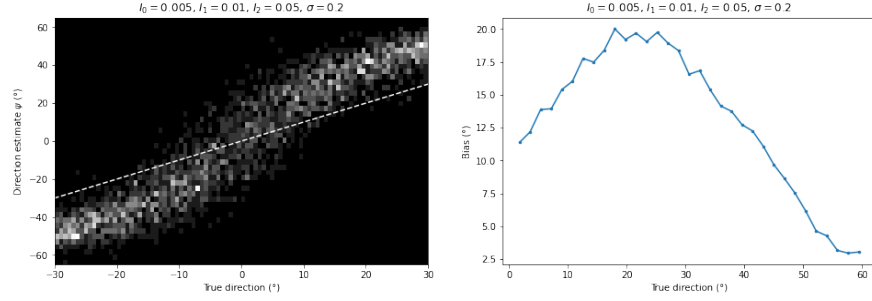


(c) Scatter plot and psychometric curve for medium coherence and a sixth Fourier order input.

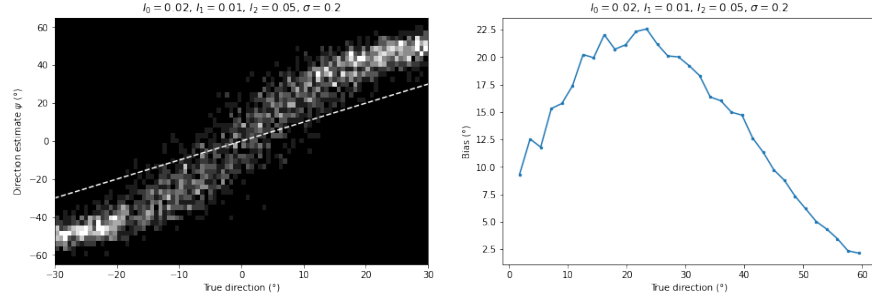


(d) Scatter plot and psychometric curve for high coherence and a sixth Fourier order input.

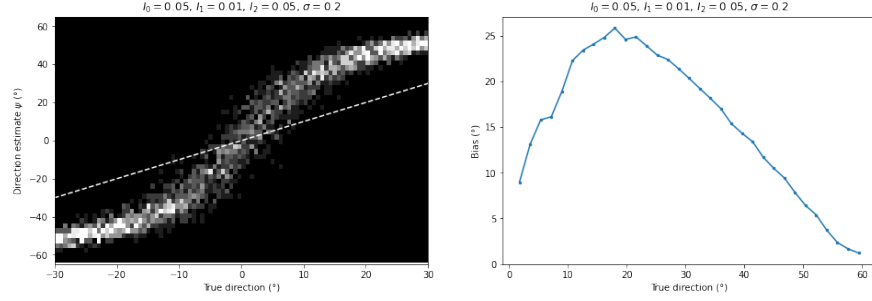
Figure C.1: Figures representing the distribution of estimation responses and psychometric curves for one subject at the three coherence levels. Each column of each plot represents the distribution of estimates for a particular true direction of motion.



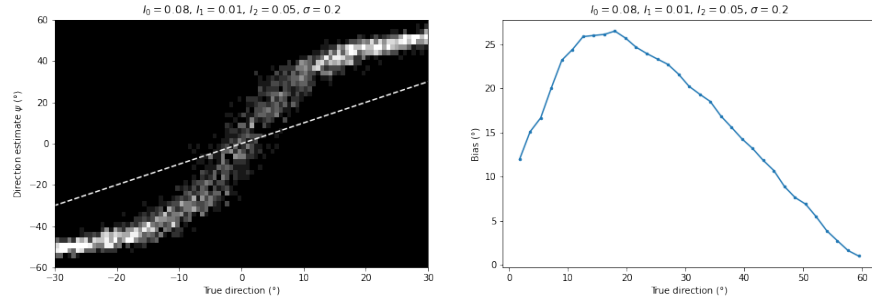
(a) Density and bias plot for very low coherence and a sixth Fourier order input.



(b) Density and bias plot for low coherence and a sixth Fourier order input.

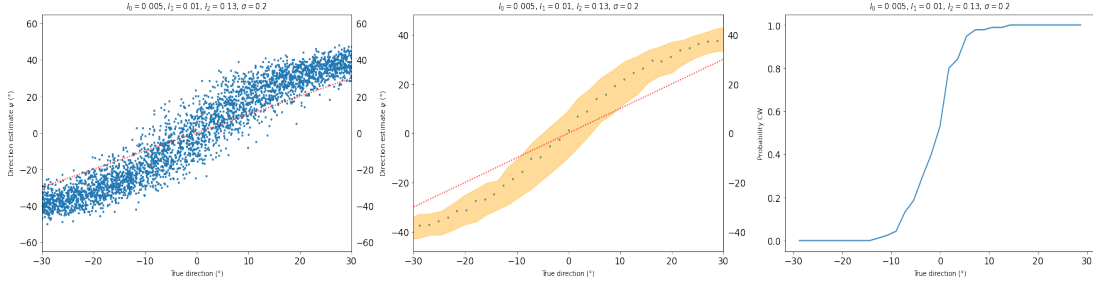


(c) Density and bias plot for medium coherence and a sixth Fourier order input.

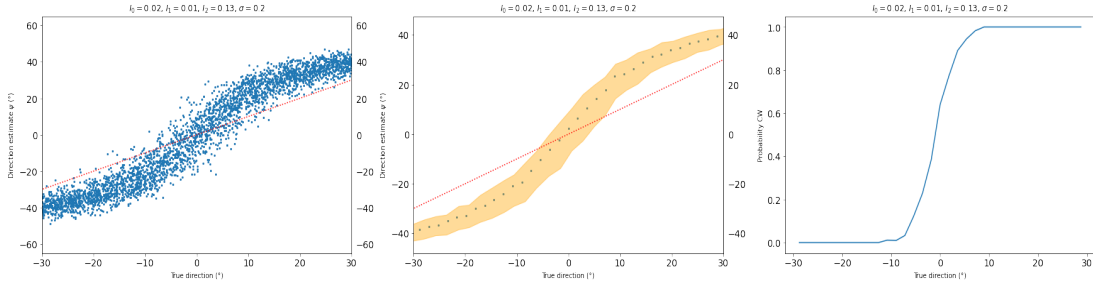


(d) Density and bias plot for high coherence and a sixth Fourier order input.

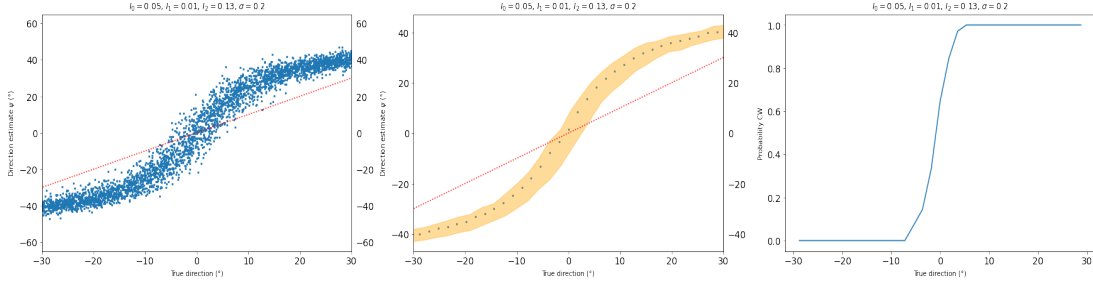
Figure C.2: Figures representing the distribution of estimation responses and bias for one subject at the three coherence levels. Each column of each plot represents the distribution of estimates for a particular true direction of motion.



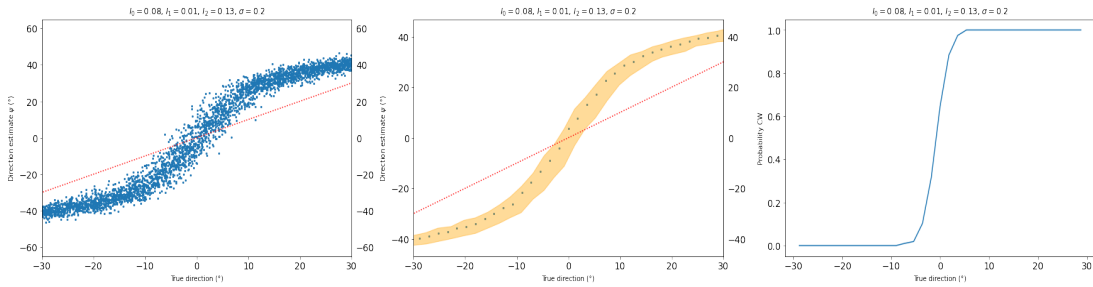
(a) Scatter plot and psychometric curve for very low coherence and a fourth Fourier order input.



(b) Scatter plot and psychometric curve for low coherence and a fourth Fourier order input.

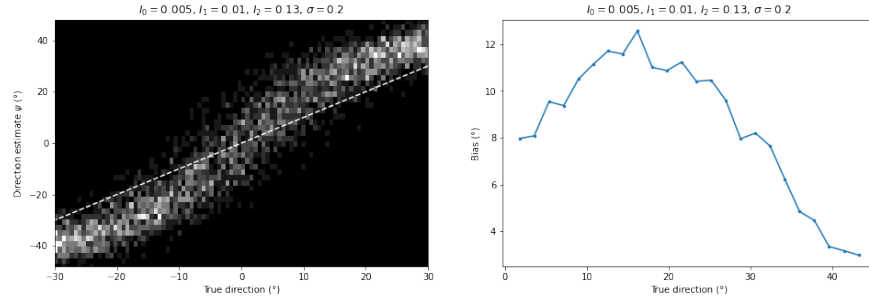


(c) Scatter plot and psychometric curve for medium coherence and a fourth Fourier order input.

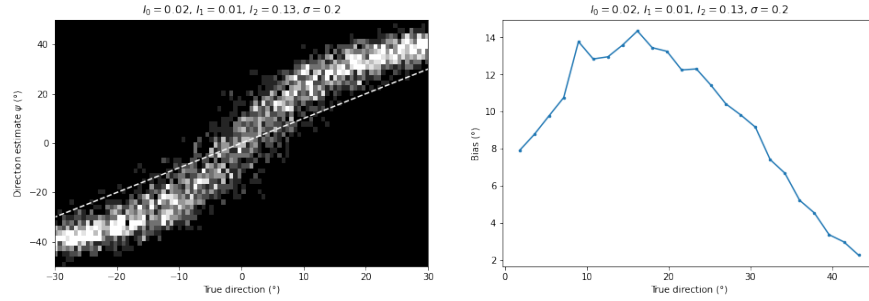


(d) Scatter plot and psychometric curve for high coherence and a fourth Fourier order input.

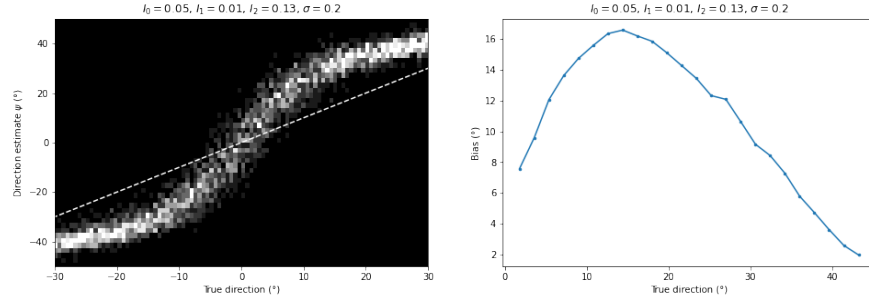
Figure C.3: Figures representing the distribution of estimation responses and psychometric curves for one subject at the three coherence levels. Each column of each plot represents the distribution of estimates for a particular true direction of motion.



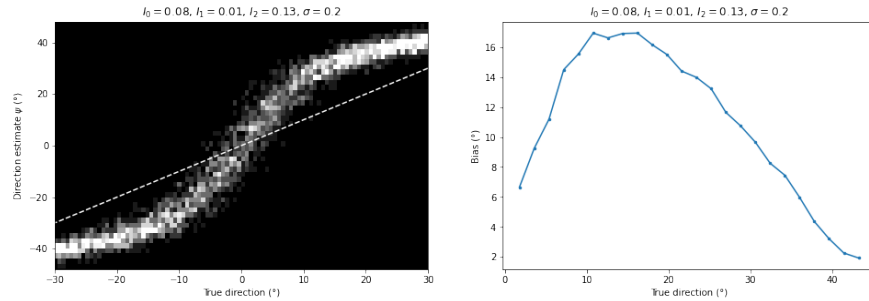
(a) Density and bias plot for very low coherence and a fourth Fourier order input.



(b) Density and bias plot for low coherence and a fourth Fourier order input.

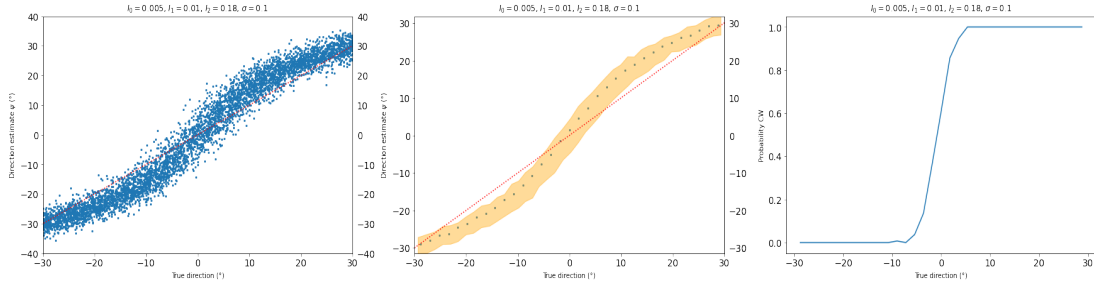


(c) Density and bias plot for medium coherence and a fourth Fourier order input.

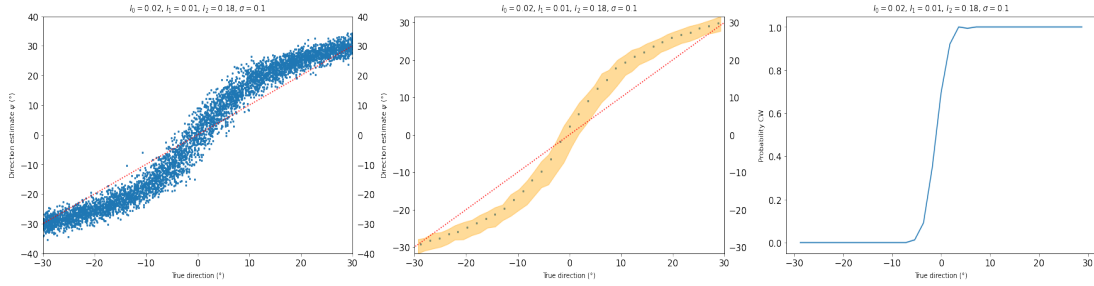


(d) Density and bias plot for high coherence and a fourth Fourier order input.

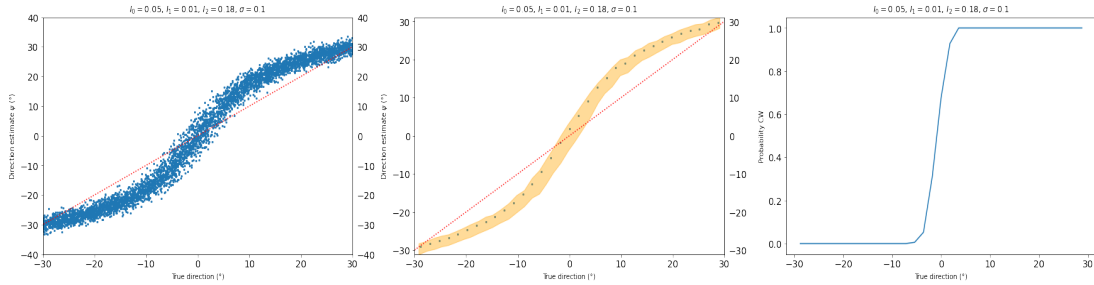
Figure C.4: Figures representing the distribution of estimation responses and bias for one subject at the three coherence levels. Each column of each plot represents the distribution of estimates for a particular true direction of motion.



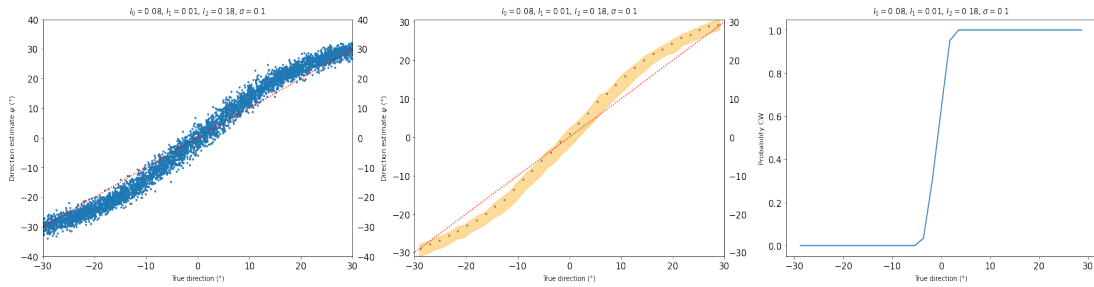
(a) Scatter plot and psychometric curve for very low coherence and a sixth Fourier order input.



(b) Scatter plot and psychometric curve very low coherence and a sixth Fourier order input.

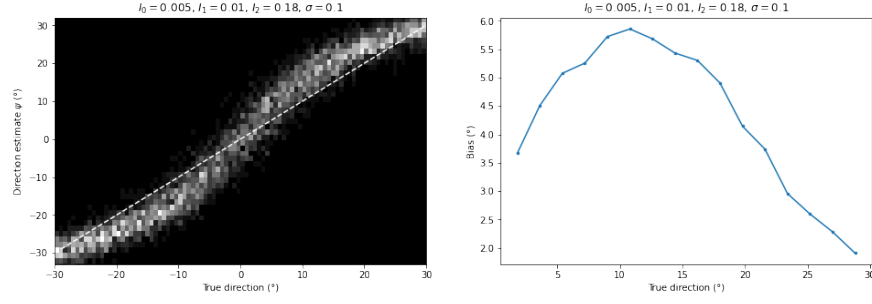


(c) Scatter plot and psychometric curve for medium coherence and a sixth Fourier order input.

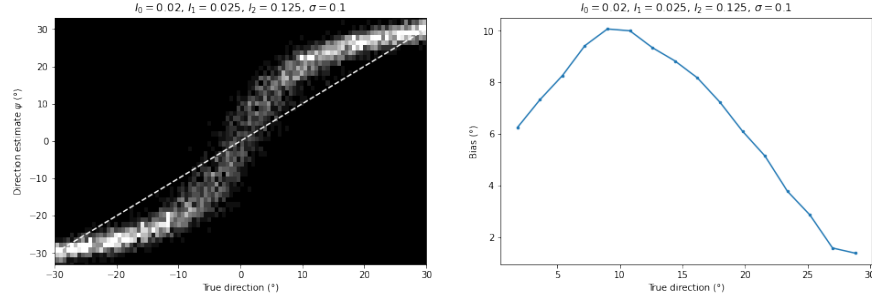


(d) Scatter plot and psychometric curve for high coherence and a sixth Fourier order input.

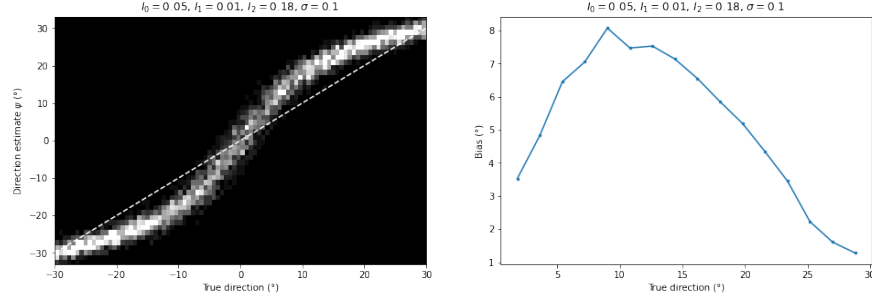
Figure C.5: Figures representing the distribution of estimation responses for one subject and a psychometric curve at the three coherence levels. Each column of each plot represents the distribution of estimates for a particular true direction of motion.



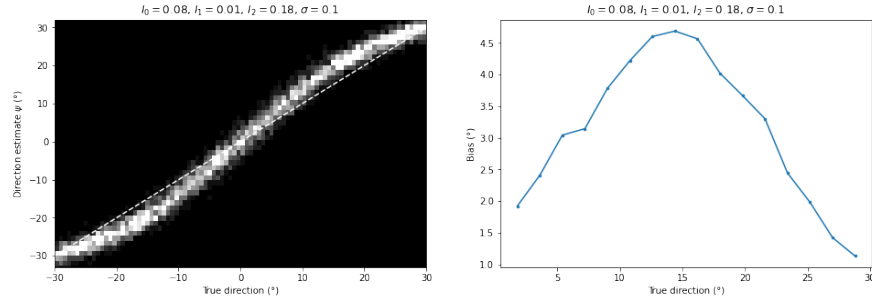
(a) Density and bias plot for very low coherence and a sixth Fourier order input.



(b) Density and bias plot for low coherence and a sixth Fourier order input.



(c) Density and bias plot for medium coherence and a sixth Fourier order input.



(d) Density and bias plot for high coherence and a sixth Fourier order input.

Figure C.6: Figures representing the distribution of estimation responses and bias for one subject at the three coherence levels. Each column of each plot represents the distribution of estimates for a particular true direction of motion.

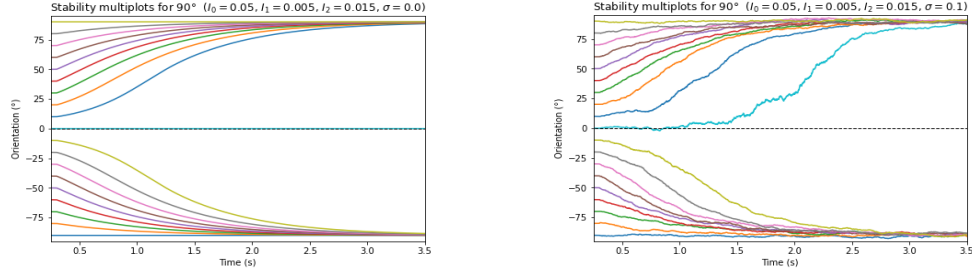


Figure C.7: Stability plot of the phase of the bump for a second order Fourier mode stimulus, $\cos\left(2\left(\theta - \frac{\pi}{2}\right)\right)$, without and with noise.

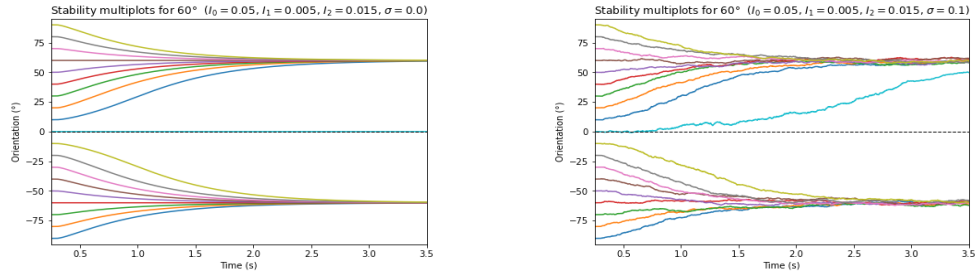


Figure C.8: Stability plot of the phase of the bump for a third order Fourier mode stimulus, $\cos\left(3\left(\theta - \frac{\pi}{3}\right)\right)$, without and with noise.

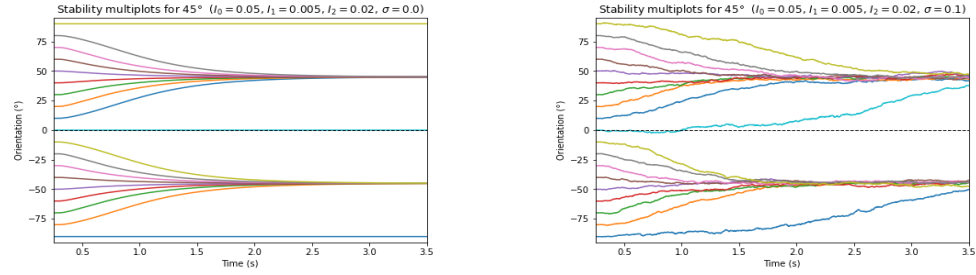


Figure C.9: Stability plot of the phase of the bump for a fourth order Fourier mode stimulus, $\cos\left(4\left(\theta - \frac{\pi}{4}\right)\right)$, without and with noise.

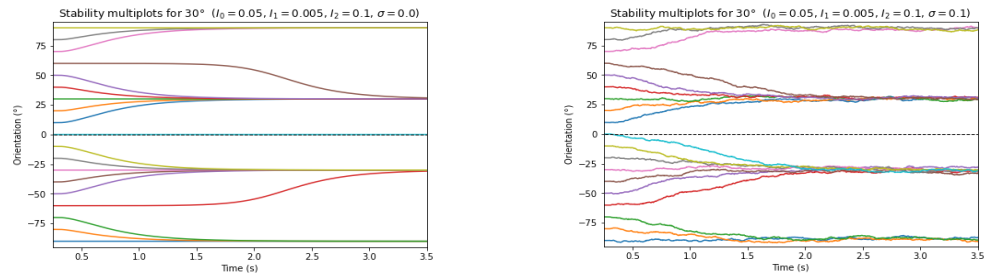


Figure C.10: Stability plot of the phase of the bump for a sixth order Fourier mode stimulus, $\cos\left(6\left(\theta - \frac{\pi}{6}\right)\right)$, without and with noise.

APPENDIX D

Code

```
import numpy as np
import math
import matplotlib.pyplot as plt
import matplotlib.colors as mcolors
import pandas as pd
import matplotlib.cm as cm
from scipy.signal import lfilter
from scipy.optimize import curve_fit
from scipy import stats
from scipy.stats import logistic, circmean, vonmises, circstd
import random

def connectivity(n, modes):
    """Creates a (('n' x 'n') connectivity matrix for the ring neural
        field model.

    :param int n: number of rate neurons/population.
    :param collections.Iterable[float] modes: amplitude of the modes of
        connectivity ordered from 0 to n_modes.
    :return: connectivity matrix.
    :rtype: np.ndarray
    """

    [i_n, j_n] = np.meshgrid(range(n), range(n))
    ij = (i_n - j_n) * (2.0 * np.pi / n)

    jphi = 0
```

```

for k, mode in enumerate(modes):
    if k == 0:
        jphi = mode
    else:
        jphi += 2.0 * mode * np.cos(k * ij)

return jphi

# Transfer function (scalar)

def sigmoid_pw(x, a=0.0000, **kwargs):
    """Piece-wise transfer function, scalar version.

    :param float x: input current
    :param float a: optional minimal firing rate (default = 0)
    :param kwargs: processed keyword arguments ('tau', 'gamma').
    :return: firing rate response.
    :rtype: float
    """

    if isinstance(x, (list, np.ndarray)):
        return sigmoid_pw_v(x, a, **kwargs)
    tau = kwargs.get('tau', 1.0)
    gamma = kwargs.get('gamma', 1.0)
    if x <= 0.0:
        return a * gamma / tau
    elif 0.0 < x < 1.0:
        return (a + x ** 2.0) * gamma / tau
    else:
        return (a + 2.0 * np.sqrt(x - 3.0 / 4.0)) * gamma / tau

# Transfer function (vectorial)

def sigmoid_pw_v(x, a=0.0000, **kwargs):
    """Piece-wise transfer function, vectorial version.

    :param np.ndarray of float x: input current
    :param float a: optional minimal firing rate (default = 0)
    :param kwargs: processed keyword arguments ('tau', 'gamma').
    :return: firing rate response.
    :rtype: np.ndarray of float
    """

    if not isinstance(x, (list, np.ndarray)):
        return sigmoid_pw(float(x), a, **kwargs)
    tau = kwargs.get('tau', 1.0)
    gamma = kwargs.get('gamma', 1.0)

```

```

    phi = x * 1.0
    # Conditions:
    m1 = (x <= 0.0)
    m3 = (x >= 1.0)
    m2 = ~(m1 | m3)
    # Function
    phi[m1] = a
    phi[m2] = a + x[m2] ** 2
    phi[m3] = a + 2.0 * np.sqrt(x[m3] - 3.0 / 4.0)

    return phi * gamma / tau

def ou_process(dt, nsteps, mu, sigma, tau, trials=1, n_spatial=1, seed=None):
    """ Generates an approximation of a single (or trials) Ornstein-Uhlenbeck
        process(es)
        for a single (oumodes) units.

    :param float dt: integration time-step.
    :param int nsteps: number of time steps.
    :param float mu: offset of the processs.
    :param float sigma: standard deviation of the process.
    :param float tau: time scale of the process (< dt).
    :param int trials: number of processes to be generated (trials).
    :param int n_spatial: number of spatially distributed units or modes of
        Fourier.
    :param int or None seed: seed for the random number generator.
    :return: time series: array (nsteps x trials x oumodes).
    :rtype: np.ndarray
    """

    # Constants
    a = np.exp(-dt / tau)
    b = mu * (1.0 - a)
    c = sigma * np.sqrt(1.0 - a ** 2)

    if seed is not None:
        np.random.seed(seed)

    s = lfilter(np.ones(1), [1, -a], b + c * np.random.randn(nsteps, trials,
        n_spatial), axis=0)

    return s

def compute_phase(x, n, c=(0.0,), s=(0.0,), wavenumber=1):
    """ Function that gives an approximate value of the phase of a spatial

```

```

    profile by projecting the vector x
    into a cosine function.

:param Cython.Include.numpy.ndarray x: firing rates matrix (or vector)
    with shape (d1, d2, ..., n).
:param int n: spatial dimension (spatial discretization).
:param np.ndarray of float c: cosine function, precompute it for faster
    computation.
:param np.ndarray of float s: sine function, precompute it for faster
    computation.
:param int wavenumber: wavenumber of the corresponding phase that we want
    to compute.
:rtype: np.ndarray of float
"""

# Check external cosine and sine functions
if len(c) != n or len(s) != n:
    c = np.cos(np.arange(n) * wavenumber * 2.0 * np.pi / n - np.pi)
    s = np.sin(np.arange(n) * wavenumber * 2.0 * np.pi / n - np.pi)

# norm of sine and cosine functions depends on n (discretization of the
# space)
return np.arctan2((np.dot(x, s) / (n / 2.0) ** 2), (np.dot(x, c) / (n /
2.0) ** 2))

def compute_estimation(dataframe, nbins=41, xlabel='theta',
    ylabel='theta_est', **kwargs):
    """ Computes the estimation curve given an angular binning with 'nbins'
    bins.

:param pd.DataFrame dataframe: data-frame containing the circular mean of
    the stimulus orientation along with
        its estimation by the model.
:param int nbins: number of bins to divide the angular range and perform
    the average across trials.
:param str ylabel: label of the outcome column in the data-frame.
:param kwargs: additional keyword arguments.
:return: Returns a tuple (binning: average stimulus orientation, average
    estimation, standard error).
:rtype: (pd.Series, pd.Series, pd.Series)
"""

    lim = kwargs.pop('lim', np.pi/2)
    # We define the categories for the data points and the model points/line
    dataframe['bin'] = equalbins(dataframe[xlabel], nbins)
    # Group the data by the binning and compute the circular mean of the

```

```

        stimulus orientation averages and the
        # circular mean of the estimated average orientations
        gby_bin = dataframe.groupby('bin')
        x_avg = gby_bin[xlabel].apply(circmean, low=-np.pi, high=np.pi)
        y_avg = gby_bin[ylabel].apply(circmean, low=-np.pi, high=np.pi)
        y_std = gby_bin[ylabel].apply(circstd, low=-np.pi, high=np.pi)
        # Select the data inside the desired range
        s_x = x_avg.loc[np.abs(x_avg) <= lim]
        s_y = y_avg.loc[np.abs(x_avg) <= lim]
        s_e = y_std.loc[np.abs(x_avg) <= lim]
        return s_x, s_y, s_e

```

```

# Define some variables
tstim = 3.500
nstim = 4
tmax = nstim * tstim # Maximum time
dt = 2E-4 # Time step
tau = 20E-3 # Neurons' time constant
n = 200 # Number of neurons in the ring network
ntrials = 1

tpoints = np.arange(0, tmax, dt)
theta = np.arange(n) / n * (2 * np.pi) - np.pi
rsteps = len(tpoints)

r = np.ones((rsteps, n)) * 0.1
phase = np.zeros(rsteps)

exc_drive = 0.05
i0 = 1 + exc_drive # Increase this to obtain the bump (supercritical bump, it
                    # grows as sqrt(i0), and its dynamics are very slow near i0 = 1)
i1 = 5E-3
i2 = 25E-3

theta_stim = np.array([30, 10, -5, 20]) * np.pi / 180 # angular direction of
                 # the stimulus (set of 8 Gabor patches)
gabor_patch = i1 * np.cos(1 * (np.repeat(theta[np.newaxis,:], nstim, axis=0)
    - theta_stim[:, np.newaxis]))

modes = [-2.0, 1.0, .5, .5, .5, .5, .5]
cnt = connectivity(n, modes)
dec_mode = 1

mu, sigmaou, tau_ou = 0, 0.10, 1E-3
ou = ou_process(dt, rsteps, 0.0, sigmaou, tau_ou, ntrials, n) # (stim_steps,
    ntrials, n), seed=None

```

```

# Loop
tstep = 0
temps = 0.0
ttautau = dt / tau

while temps < tmax:
    i_stim = gabor_patch[np.floor(temps / (tmax / nstim)).astype(int)]

    # Time step variables
    kp = tstep % rsteps #kp is the 0 step
    k = (tstep + rsteps - 1) % rsteps #k is the -1 step

    # 2. Presynaptic inputs
    s = 1.0 / n * np.dot(r[k], cnt)

    #3. Integration
    try:
        r[kp] = r[k] + ttau * (-r[k] + sigmoid_pw_v(i0 + i_stim + tau * s +
            ou[kp], tau=tau))
        phase[kp] = compute_phase(r[kp], n)
    except FloatingPointError: # Prevent UnderFlow errors by setting the
        firing rate to 0.0
        r[r < 1E-12] = 0.0

    tstep += 1
    temps = tstep * dt

if dec_mode == 1:

    # Reset some variables
    tbias = 1.500
    tpoints_bias = np.arange(0, tbias, dt)
    rsteps_bias = len(tpoints_bias)

    r = np.concatenate((r, np.ones((rsteps_bias, n)) * 0.1))
    phase = np.concatenate((phase, np.zeros(rsteps_bias)))

    tstep = 0
    temps = 0.0

    i_stim = i2 * np.cos(180/30 * (theta - np.pi/180 * 30))
    ou = ou_process(dt, rsteps_bias, mu, sigmaou, tau_ou, ntrials, n) #
        (stim_steps, ntrials, n) seed=None

    while temps < tbias:

```

```

# Time step variables
kp = tstep % rsteps_bias + rsteps #kp is the 0 step
k = (tstep + rsteps_bias - 1) % (rsteps_bias - 1) + (rsteps - 1) #k is
    the -1 step

# 2. Presynaptic inputs
s = 1.0 / n * np.dot(r[k], cnt)

# 3. Integration
try:
    r[kp] = r[k] + ttau * (-r[k] + sigmoid_pw_v(i0 + i_stim + tau * s
        + ou[kp - rsteps], tau=tau))
    phase[kp] = compute_phase(r[kp], n)
except FloatingPointError: # Prevent UnderFlow errors by setting the
    firing rate to 0.0
    r[r < 1E-12] = 0.0

tstep += 1
temps = tstep * dt

```

For more information about how these different chunks of code are applied and which necessary parts are missing for the statistical analysis, you can access the [Github](#) repository I have created.

Bibliography

- [1] R. Ben-Yishai, R. L. Bar-Or, and H. Sompolinsky. “Theory of orientation tuning in visual cortex”. In: *PNAS* 92.9 (1995), pp. 3844–3848. DOI: <https://doi.org/10.1073/pnas.92.9.3844>.
- [2] Jose M. Esnaola Acebes. “Patterns of spike synchrony in neural field models”. PhD thesis. Universitat Pompeu Fabra, 2018. DOI: <https://www.tdx.cat/bitstream/handle/10803/663871/tjmea.pdf?sequence=5.xml>.
- [3] Jose M. Esnaola-Acebes, Alex Roxin, and Klaus Wimmer. “Bump attractor dynamics underlying stimulus integration in perceptual estimation tasks”. In: *bioRxiv* (2021). DOI: [10.1101/2021.03.15.434192](https://doi.org/10.1101/2021.03.15.434192). URL: <https://www.biorxiv.org/content/early/2021/08/09/2021.03.15.434192>.
- [4] Wulfram Gerstner et al. *Neuronal Dynamics: From Single Neurons to Networks and Models of Cognition*. USA: Cambridge University Press, 2014. ISBN: 1107635195.
- [5] D. Hansel and H. Sompolinsky. *Modeling Feature Selectivity in Local Cortical Circuits*. Methods in Neuronal Modeling: From Ions to Networks, 1998, pp. 499–567.
- [6] Eugene M. Izhikevich. *Dynamical Systems in Neuroscience: The Geometry of Excitability and Bursting*. The MIT Press, 2006. DOI: <https://doi.org/10.7551/mitpress/2526.001.0001>.
- [7] M. Jazayeri and J Movshon. “A new perceptual illusion reveals mechanisms of sensory decoding”. In: *Nature* 446 (2007), pp. 912–915. DOI: [10.1038/nature05739](https://doi.org/10.1038/nature05739).
- [8] M. Jazayeri and J Movshon. “Optimal representation of sensory information by neural populations”. In: *Nature Neuroscience* 9 (2006), pp. 690–696. DOI: <https://doi.org/10.1038/nn1691>.
- [9] Yoshiki Kuramoto. *Chemical Oscillations, Waves, and Turbulence*. Springer Berlin, Heidelberg, 1984. DOI: <https://doi.org/10.1007/978-3-642-69689-3>.

- [10] H.R. Wilson and J.D. Cowan. “A mathematical theory of the functional dynamics of cortical and thalamic nervous tissue”. In: *Kybernetik* 13 (Sept. 1973), pp. 55–80.
DOI: <https://doi.org/10.1007/BF00288786>.

Declaració d'autoria del Treball Final de Grau

Jo, Miguel Donderis de Vicete, amb Document Nacional d'Identitat 29221379V, i estudiant del Grau en Física de la Universitat Autònoma de Barcelona, en relació amb la memòria del Treball Final de Grau presentada per a la seva defensa i avaluació durant la convocatòria de setembre del curs 2021-2022, declara que

- El document presentat és original i ha estat realitzat per la seva persona.
- El treball s'ha dut a terme principalment amb l'objectiu d'avaluar l'assignatura de Treball Final de Grau en física en la UAB, i no s'ha presentat prèviament per ser qualificat en l'avaluació de cap altra assignatura ni en aquesta ni en cap altra universitat.
- En el cas de continguts de treballs publicat per terceres persones, l'autoria està clarament atribuïda, citant les fonts degudament.
- En el casos en els que el meu treball s'ha realitzat en col·laboració amb altres investigadors i/o estudiants, es declara amb exactitud quines contribucions es deriven del treball de tercers i quines es deriven de la meva contribució.
- A excepció del punts esmentats anteriorment, el treball presentat és de la meva autoria.

Signat:

Miguel Donderis de Vicente

Bellaterra, 15 d'agost de 2022

Declaració d'extensió del Treball Final de Grau

Jo, Miguel Donderis de Vicente, amb Document Nacional d'Identitat 29221379V, i estudiant del Grau en Física de la Universitat Autònoma de Barcelona, en relació amb la memòria del Treball Final de Grau presentada per a la seva defensa i avaluació durant la convocatòria de setembre del curs 2021-2022, declara que:

- El nombre total de paraules (segons comptatge proposat) incloses en les seccions des de la introducció fins a les conclusions és de 7011 paraules.
- El nombre total d'equacions és de 63, el que comptabilitza un total de $63 \times 20 = 1260$ paraules
- El nombre total de figures és de: 1 figura, 1 figura amb dues subfigures, 1 figura amb 4 subfigures i 1 figura amb 6 subfigures, comptabilizant un total de $200 + 200 + 400 + 600 = 1400$ paraules.

En total el document, comptabilitza:

$$7011 + 1260 + 1400 = 9871 \text{ paraules,}$$

que compleix amb la normativa al ser inferior a 10000 paraules.

Signat:

Miguel Donderis de Vicente

Bellaterra, 15 d'agost de 2022